

Post-print version of:

Publisher: **Elsevier**

Journal paper: **International Journal of Fatigue, 2023, 174, 107713**

Title: **Elastic–plastic analysis of high load ratio fatigue tests on a shot-peened quenched and tempered steel, combining the Chaboche model and the Theory of Critical Distances**

Authors: **C. Santus, L. Romanelli, T. Grossi, L. Bertini, L. Le Bone, F. Chiesi, L. Tognarelli.**

Creative Commons Attribution Non-Commercial No Derivatives License



DOI Link: <https://doi.org/10.1016/j.ijfatigue.2023.107713>

Highlights

Elastic-plastic analysis of high load ratio fatigue tests on a shot-peened quenched and tempered steel, combining the Chaboche model and the Theory of Critical Distances

Ciro Santus, Lorenzo Romanelli, Tommaso Grossi, Leonardo Bertini, Luca Le Bone, Francesco Chiesi, Leonardo Tognarelli

- Chaboche kinematic hardening rule to model the cyclic plastic behaviour.
- Residual stresses after the shot peening reproduced with the eigenstrain technique.
- Residual stresses after fatigue modelled with an increase of the material hardening.
- Smith-Watson and Topper combined with The Theory of Critical Distances.
- Low prediction errors of the fatigue strength assessment.

Elastic-plastic analysis of high load ratio fatigue tests on a shot-peened quenched and tempered steel, combining the Chaboche model and the Theory of Critical Distances

Ciro Santus^a, Lorenzo Romanelli^{a,*}, Tommaso Grossi^a, Leonardo Bertini^a, Luca Le Bone^b, Francesco Chiesi^b and Leonardo Tognarelli^b

^aDICI, Department of Civil and Industrial Engineering, University of Pisa, Largo Lucio Lazzarino 1 - 56122, Pisa, Italy

^bBaker Hughes - Nuovo Pignone, Via Felice Matteucci 2 - 50127, Florence, Italy

ARTICLE INFO

Keywords:

Theory of Critical Distances

Chaboche kinematic hardening model

Residual stresses

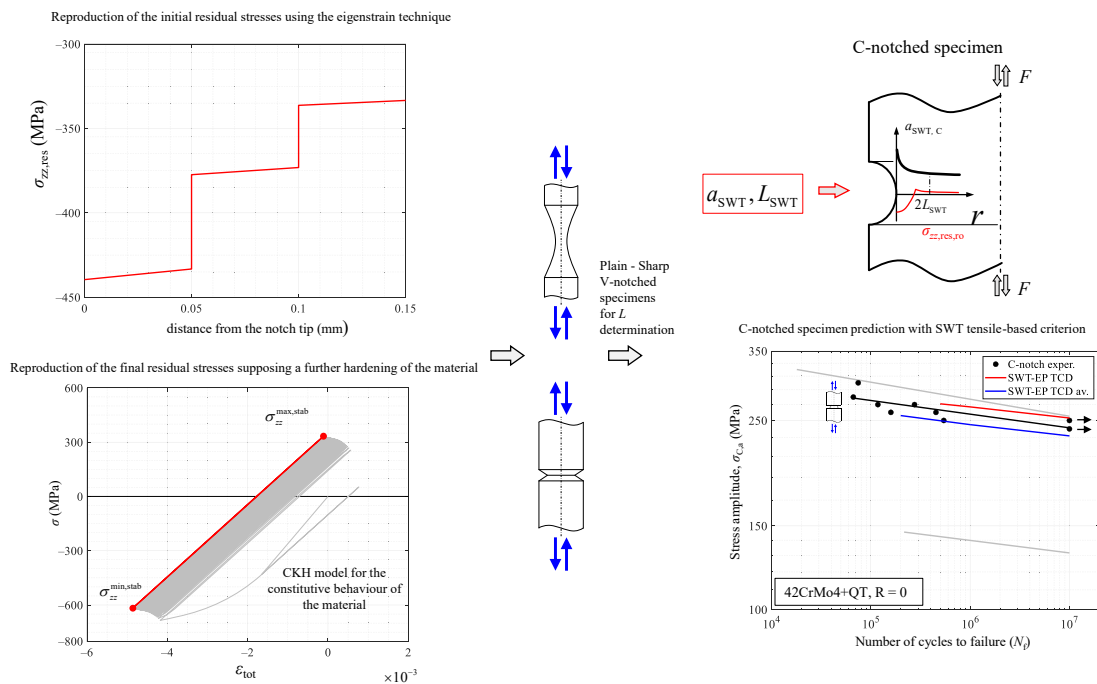
Eigenstrain technique

Smith-Watson and Topper model

ABSTRACT

This study aimed to predict the uniaxial fatigue strength of shot peened notched specimens made of 42CrMo4 quenched and tempered steel. The Chaboche kinematic hardening rule was employed to model the cyclic plastic behaviour of the tested samples and the evolution of the residual stresses, which were measured with X-ray diffraction and then reproduced through a finite element software with a novel proposed procedure. This latter introduced a distribution of eigenstrains to reproduce the initial residual stresses and a hardening of the material to replicate the residual stresses measured after the loading for a run-out specimen. The Theory of Critical Distances combined with the Smith-Watson and Topper multiaxial fatigue criterion were then employed to predict the fatigue strength resulting in a good level of accuracy.

Graphical Abstract



lorenzo.romanelli@phd.unipi.it (L. Romanelli)

ORCID(s): 0000-0003-0859-626X (C. Santus); 0000-0001-6484-5051 (L. Romanelli); 0000-0002-2756-2893 (T. Grossi); 0000-0003-1618-7845 (L. Bertini)

Nomenclature

TCD	Theory of Critical Distances
LM, PM	Line Method and Point Method, respectively
EP	elastic-plastic material behaviour
El	linear elastic material model
FE	finite element
SWT	Smith-Watson-Topper criterion
MWCM	Modified Whöler Curve Method
FS	Fatemi-Socie criterion
ERM	Eigenstrain Reconstruction Method
CPZ	Cyclic plastic zone
P_i	point on the notched samples bisector where the residual stresses were measured
P'_i	point on the plain sample bisector where the residual stresses were measured
d_i	distance from the notch tip of the points where the residual stresses were measured
ΔK_{th}	threshold stress intensity factor range
$\Delta\sigma_0$	plain specimen fatigue limit range
L	critical distance according to the LM, mode I (axial loading)
L_T	critical distance according to the LM, mode III (torsional loading)
D	diameter of the collimator used during the measures of the residual stresses
χ	tilt angle of the XRD $\sin^2\psi$ technique and the modified χ method
2θ	the diffraction angle of the XRD $\sin^2\psi$ and the modified χ technique
σ_{zz}	axial stress
$\sigma_{\theta\theta}$	circumferential stress
$\sigma_{zz}^{max,stab}, \sigma_{zz}^{min,stab}$	maximum and minimum axial stress of the stabilized cycle reached during the fatigue loading
ϵ_{tot}	total strain
ϵ_p	plastic component of the total strain
R	fatigue stress load ratio
R_ϵ	fatigue strain load ratio
$\sigma_{a,fl}$	plain specimen fatigue limit, axial loading amplitude
$\sigma_{V,a,fl}$	V-notched specimen fatigue limit, nominal axial loading amplitude
$\sigma_{C,a,fl}$	C-notched specimen fatigue limit, nominal axial loading amplitude
$\sigma_a, \sigma_{V,a}, \sigma_{C,a}$	normal stress amplitudes of the specimens plain, V-notched and C-notched (nominal)
N_f	Number of cycles to failure
σ_L	Chaboche kinematic hardening model elastic limit
C_i, γ_i	Backstress parameters of the Chaboche kinematic hardening model
$\{\sigma_{res}\}$	vector containing the initial residual stresses at point P_i
$\sigma_{zz,res,i}$	axial initial residual stress at point P_i
$\sigma_{\theta\theta,res,i}$	circumferential initial residual stress at point P_i
$\{\sigma_{zz,res,i}(P_i)\}$	difference vector between the experimental and the modelled residual stresses after fatigue loading
$\{\alpha\}$	vector containing the eigenstrains to reproduce the initial residual stresses
$\alpha_{zz,i}$	Coefficient of thermal expansion in the z direction for the area A_i
$\alpha_{\theta\theta,i}$	coefficient of thermal expansion in the θ direction for the area A_i
\mathbf{K}	stiffness matrix involved in the reproduction of the initial residual stresses
ΔT	set temperature variation through FEM to reproduce the initial residual stresses
\mathbf{J}	iterative matrix involved in the reproduction of the final residual stresses
$\sigma_{zz,res,ro}$	axial residual stresses measured on the run-out specimen
$\Delta\sigma_{zz,res,ro}(P_i)$	calculated increment of axial residual stress after fatigue loading matrix to populate matrix \mathbf{J}
$\sigma_{zz,res,ro}^s(P_i)$	modelled axial residual stress in point P_i after fatigue loading at the step s of the iterative procedure
$\Delta\sigma_L$	increase of the Chaboche elastic limit to reproduce the final residual stresses
$\{\sigma_L(A_i)\}$	vector containing the value of the Chaboche elastic limit corresponding to the area A_i
$\{\sigma_L(A_i)\}_s$	vector containing the modelled value of the Chaboche elastic limit of the area A_i at the step s

$\sigma_L(A_i)$	value of the Chaboche elastic limit corresponding to the area A_i
$\{\delta\sigma_L(A_i)\}$	vector containing the increment of the Chaboche elastic limit of the area A_i
ε_a	normal strain amplitude for the SWT criterion
$\varepsilon_{pl,a}, \varepsilon_{V,a}, \varepsilon_{C,a}$	normal strain amplitude of the specimens plain, V-notched and C-notched for the SWT criterion
σ_n^{\max}	maximum normal stress on the critical plane
$\sigma_{n,pl}^{\max}, \sigma_{n,V}^{\max}, \sigma_{n,C}^{\max}$	maximum normal stress on the critical SWT planes of the specimens plain, V-C-notched
S_Y	Yield stress
S_U	Ultimate stress
ΔL	Elongation at fracture
a_{SWT}	SWT fatigue parameter
$a_{SWT,pl}, a_{SWT,V}, a_{SWT,C}$	SWT fatigue parameter of the plain, V-notched and C-notched specimens
$a_{SWT,av}$	SWT fatigue parameter obtained from the averaged critical distance
L_{SWT}	LM length according to the SWT criterion
$L_{SWT,av}$	averaged LM length according to the SWT criterion

1. Introduction

Neuber in his precursory work discussed that the damage at the notch tip is not well represented by the stresses predicted with the continuum mechanics [1, 2]. To have a quantity to describe the fatigue damage of notched components, he suggested averaging the stress near the notch over a material unit. Similarly, Peterson later suggested in [3] that the quantity representative of the fatigue damage of notched components is the stress value at a certain distance from the apex of the stress raiser. These considerations of Neuber and Peterson were formalized by Taylor in [4] by proposing the Theory of Critical Distances (TCD) and in particular the Line Method (LM) and the Point Method (PM). The LM proposes that the notch effect on the fatigue strength is captured by averaging the stress amplitude distribution along the notch bisector over the distance $2L$. On the other hand, the PM just takes into account the stress evaluated on the notch bisector and at a distance of $L/2$ from the notch tip. The value of L depends on the material, the load ratio and the number of cycles to failure. Initially, Taylor postulated this theory considering a purely elastic behaviour of the material and a uniaxial (remote) loading. In agreement with this, the length L turns out the same as proposed by Haddad et. al. [5]:

$$L = \frac{1}{\pi} \left(\frac{\Delta K_{th}}{\Delta \sigma_0} \right)^2 \quad (1)$$

where ΔK_{th} is the mode I threshold stress intensity factor range and $\Delta \sigma_0$ is the fatigue strength of the plain specimen. Recently, Santus et al. [6, 7] proposed an optimized V-notched specimen to alternatively obtain the value of L . The severe gradient provided by the V-notched sample, combined with the fatigue limit of the plain specimen, does not require the determination of the threshold stress intensity factor range. This proposal was applied in a modified form by Benedetti et al. [8], where two specimens with different notch severity were employed to calculate the value of L . The TCD was extended to torsional loadings by Susmel et al. [9, 10]. The critical distance related to torsional loadings was also investigated by Santus et al. [11]; an optimized V-notched specimen was proposed to calculate the value of L_T , and the experimental results led to $L_T > L$ in agreement with previous papers by Susmel et al. Given the diffusion of multiaxial fatigue criteria to assess the fatigue life of samples as in [12, 13, 14, 15, 16, 17, 18, 19, 20, 21], the TCD can be combined with more complex criteria to predict the fatigue life of components. In Santus et al. [22] the criteria of Fatemi-Socie (FS) and Smith-Watson and Topper (SWT) were combined with the LM to predict the fatigue life of notched components subjected to torsional loadings, in Liao et al. [23] the FS criterion was employed together with the LM and the PM to calculate the fatigue life of notched components under uniaxial loading and in Susmel and Taylor [24] the Modified Whöler Curve Method (MWCM) was applied together with the PM to estimate the finite life of notched components under variable amplitude uniaxial/multiaxial fatigue loadings. The TCD was also employed to predict the fatigue life of specimens obtained through additive manufacturing. For example, in [8, 25] the classical form of the LM according to [4] was applied, while in Benedetti et al. [26] the LM was combined with multiaxial fatigue criteria as FS, MWCM, Carpinteri e Spagnoli and modified SWT.

Given that in specimens with severe stress raisers the equivalent stress could overcome the elastic limit of the material, at least near the notch tip, the involvement of an elastic-plastic constitutive law allows to obtain a reliable description of the behaviour of the material. In Taddesse et al. [27] the concept of the cyclic plastic zone (CPZ), whose size depends on the material strength, was combined with the Chaboche damage evolution model [28], and a closed-form expression for fatigue analyses of notched components was obtained. In Taddesse et al. [29], the idea of the CPZ was then combined with the LM and the PM for low cycle fatigue analyses of notched components. Considering that the Bauschinger effect often occurs during the cyclic-plastic behaviour of the materials, a kinematic hardening rule should be employed to account for this phenomenon. The Chaboche kinematic hardening (CKH) model [30] is a powerful constitutive law to model the plasticity of metals, and it can be efficiently combined with Voce isotropic hardening rule [31] to account for the dependency of the elastic limit on the cumulated plastic strain. The CKH model was introduced by Chaboche, expanding the Armstrong and Frederick model [32] by adding multiple backstress components. CKH model was also efficiently used together with multiaxial fatigue criteria and TCD in [22, 33], while Armstrong and Frederick model was applied with the Strain Energy Density criterion by Branco et al. in Ref. [34]. In fracture mechanics problems, the CKH rule was also used by Paul in Refs. [35, 36] to model the cyclic plastic behaviour of the material near the crack tip. Some modifications were made to the CKH rule during the years, such as by Chaboche himself in Ref. [37], where a backstress with threshold was introduced to improve the ratcheting rate predictions. Below this threshold, the material behaves according to the linear Prager hardening rule, while it behaves according to the nonlinear CKH law above the threshold. This refinement was then improved by Chaboche et al. [38], within the context of fatigue life analyses of components experiencing small strain amplitudes but high strain ratio, to reproduce the cyclic softening and the mean stress relaxation. The determination of the CKH model parameters is a challenging task, which can be performed in different ways. In Refs. [39, 40] the determination of the CKH model parameters was carried out by engaging only stress-controlled tests, whereas in Refs. [41, 42] both uniaxial strain-controlled tests and stress-controlled tests were considered to calculate the parameters. Various algorithms were employed to compute the CKH model constants: in Mahmoudi et al. [43] and in Agius et al. [44] a genetic algorithm was used, in Moslemi et al. [45] a particle swarm optimization was employed and in Pham and Nguyen [46] a differential evolution algorithm was applied. In Santus et al. [47, 48] a procedure based on the global properties of the stabilized cycles was presented, showing a good ability to reproduce the experimental data with a low computational cost, and the parameters obtained utilizing this approach are used in the present analysis too.

The shot-peening is a well-known process to improve the fatigue strength of the mechanical components. It is widely discussed in the literature that the shot peened specimens offer an increased fatigue strength and an increase of the hardness of the shot peened zone. Discussions about the effects of shot peening on the hardness and the fatigue strength were provided by Lv et al. [49] for surface melted 20CrMnTi steel gear, by Héctor E Jaramillo et al. [50] for specimens of SAE 5160 steel, by Žagar et al. [51] for components of 7075 Aluminium alloy and by Zheng et al. [52] for components of Ti-10V-2Fe-3Al. In this latter studies, an increase of hardness of the shot peened zone with respect to the base material and an increase of the fatigue strength of the shot peened samples were observed. The effects of the classic shot-peening process were also compared with the effects of severe shot peening. This latter process resulted in higher hardness values of the shot peened zone than those obtained by classical shot peening and an improvement of the fatigue strength was also noted. These latter outcomes were described by Bagherifard et al. [53] for cast iron specimens and by Maleki et al. [54] regarding components of steel AISI 1060. After their measurements with various techniques: hole-drilling, X-ray diffraction (XRD) or neutron diffraction, the residual stresses can be reproduced through a finite element (FE) software in different ways. One strategy to model the measured residual stresses is the eigenstrain technique. The term eigenstrain was introduced by Mura in [55] indicating all the permanent strains arising in the material caused by an inelastic process, and it was indicated as the source of the residual stress. Korsunsky proposed a general method, based on a robust least squares approach, to calculate the distribution of eigenstrains to set in the FE software to reproduce the measured residual stresses. The suggested strategy was applied by Korsunsky et al. in many applications such as in shot peening [56, 57], laser shock peening [58], autofrettaged tubes [59], laser forming [60] and also in welding [61]. In Jun and Korsunsky [62], the eigenstrain reconstruction method (ERM) was then proposed. This technique consists of the residual strain measurement, the solution of the inverse problem of eigenstrain theory and the application of the Simple Triangle (SIMTRI) method. The SIMTRI strategy models the distribution of the eigenstrains by the superposition of triangular basis functions, whereas, before the ERM, Korsunsky modelled the distribution of eigenstrains with various analytical expressions as in Ref. [61] where the Chebyshev polynomials were employed. According to these authors, the employment of triangular basis functions allows to obtain a more generic methodology to match the eigenstrains with the measured residual stresses. The ERM was used many times

in residual stresses problems by Salvati et al. [63] to reconstruct the residual strains in an additively manufactured and shot peened nickel superalloy compressor blade, by Achintha and Nowell [64] to model the residual stresses generated by laser shock peening, by Korsunsky et al. [65] for the description of inelastic deformation induced by focused ion beam damage in a flexible silicon cantilever and by Korsunsky et al. [66] to study the nanoscale residual stresses caused by focused ion beam milling. A similar approach to the ERM was used by Benedetti et al. [67], where the measured residual stresses in plain and shot peened specimens, made of different high-strength aluminium alloys, were reproduced. Another technique to replicate the residual stresses consists in simulating the impacts between the shots and the specimens as, for example, recently done by Marini et al. in [68]. After the correct representation of the experimental residual stresses through a FE software, multiaxial fatigue criteria can be involved to calculate the fatigue strength of shot-peened components. In Bagherifard and Guagliano [69] some fatigue criteria based on nominal and local stress were applied to notched and shot-peened specimens under different fatigue loadings and supposing a purely elastic behaviour of the material. In Benedetti et al. [70] some multiaxial fatigue criteria as Sines, Crossland, F-S, Findley and modified SWT were employed to calculate the fatigue strength of plain and shot-peened components under various fatigue loadings as pure tension, pure torsion and in-phase tension and torsion. In this latter study the constants of the criteria were calibrated on the unpeened specimens and then employed with the shot-peened specimens given that the modifications of the material due to residual stresses exerted a negligible influence on the fatigue strength. Even in this latter research, a purely elastic behaviour of the material was supposed. The effect of the residual stresses was considered through mean stresses superimposed to the oscillating stresses introduced by the external cyclic load. In Benkhettab et al. [71] a modified version of the Crossland criterion was presented by including in the criterion the measured plastic strain and the compressive stress caused by the shot-peening process. There are also some examples about the application of the TCD combined with multiaxial fatigue criteria to calculate the fatigue strength of notched and shot peened specimens. For example, in the paper by Benedetti et al. [72] the LM was applied together with the Sines multiaxial fatigue criterion, whereas in Ref. [73] the Area Method was employed together with the Crossland multiaxial fatigue criterion. Another example is the paper by Bagherifard et al. [74] in which two approaches were applied: the Aztori approach [75] and the combination between the LM and the Sines multiaxial fatigue criterion.

In the present study, the CKH rule was employed to model the elastic-plastic behaviour of notched and shot peened specimens of a quenched and tempered steel. The CKH model constants were determined according to the procedure proposed in Ref. [47] and the results of the calibration, for the steel investigated here, were presented in Ref. [48]. The residual stresses immediately after the shot-peening process, and the residual stresses for a run-out specimen at the end of the fatigue loading, were measured by means of X-Ray diffraction (XRD) and then reproduced with the FE software Ansys. The reproduction of the initial residual stresses was developed through a distribution of eigenstrains, similarly to the technique proposed by Jun and Korsunsky [62] previously mentioned, whereas the residual stresses measured at the end of the fatigue loading were only obtained by considering an increase of the hardening of the material in the initial subsurface region due to the shot peening process. After the reproduction of the residual stresses was accomplished and validated, the V-notched and the plain specimens were employed to calculate the values of the critical distances combining the LM and the SWT multiaxial fatigue criterion. C-notched specimen was used as a validator of the procedure and the values of its uniaxial fatigue strength, varying with the number of cycles, were assessed and then compared with the experimental data, and accurate fatigue strength predictions were obtained.

2. Materials

2.1. Specimen geometries and their role in the analyses

In this study four kinds of samples were involved: two types of plain specimens, one C-notched specimen and one V-notched specimen, the geometries of these specimens are shown in Fig. 1. The plain specimen (a) was used to perform the monotonic tensile test and the cyclic plastic tests to obtain the CKH model parameters. The plain specimen (b) and the V-notched specimen (c) were employed to reproduce the residual stresses obtained after the shot-peening process and to calculate the values of the critical distances. Finally, the C-notched specimen (d) was used to replicate both the residual stresses obtained after the shot-peening and the residual stresses measured at the end of the fatigue loading for a run-out specimen. The C-notched specimen was also considered for validation of the fatigue strength using the values of the critical distances calculated through the combination of the plain specimen (b) and the V-notched specimen (c).

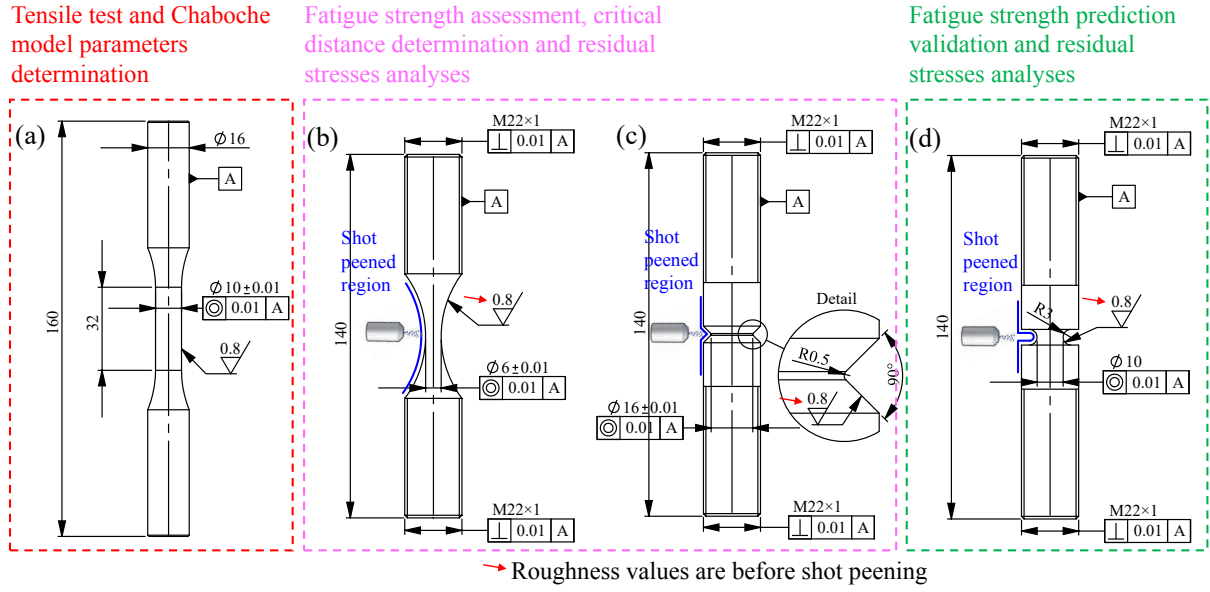


Figure 1: Technical drawings of the specimens and their use in the study.

2.2. Modelling of the elastic-plastic behaviour of the material

The material involved in this research was a 42CrMo4+QT (quenched and tempered) steel, with the following properties: $S_Y = 500 \pm 5$ MPa, $S_U = 700 \pm 5$ MPa and $\Delta L = 32\%$ respectively. The CKH rule with four backstress components was employed to model the elastic-plastic behaviour of the material. The CKH model parameters were calculated according to the procedure proposed by Santus et. al. [47], which was then applied in Ref. [48] to compute the constants of CKH model parameters regarding the steel involved in this study. The roles of the parameters according to this procedure, newly introduced by the authors, are the following:

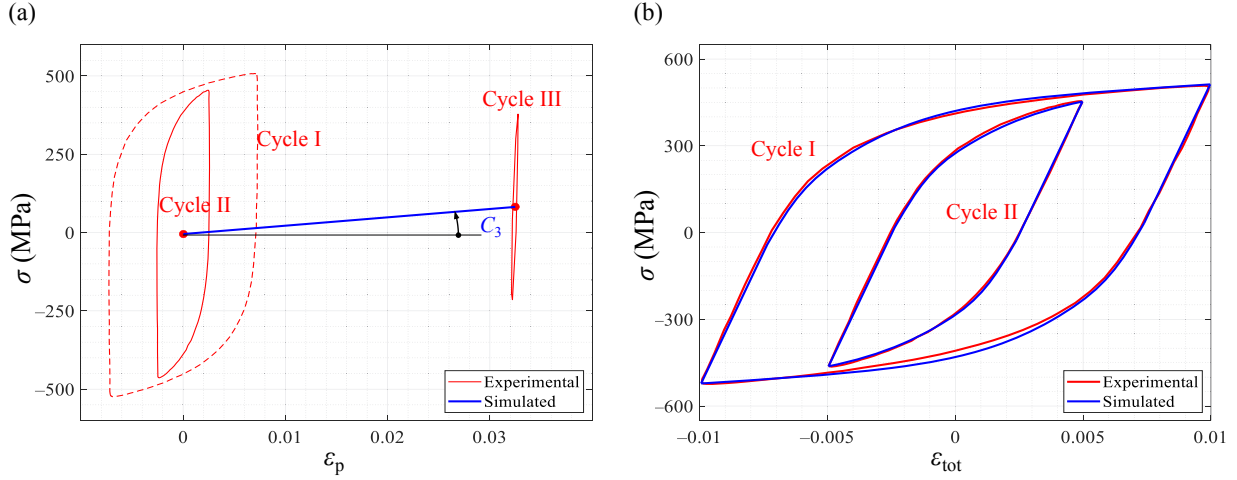
1. A linear and a slightly nonlinear backstresses: $\gamma_3 = 0$ and $\gamma_2 \ll \gamma_1$.
2. C_3 predicts the mean point of the stabilized cycle.
3. C_1 , C_2 , γ_1 and σ_L model the global properties of the stabilized cycles of the strain-controlled tests as the hysteresis area, the slope at the inversion points and the stress amplitude
4. γ_2 models the ratcheting rate.
5. And finally, a fourth backstress with a high value of γ_4 aims to improve the prediction near the elastic limit.

To develop the calculation of the parameters four experimental tests were performed: three strain-controlled tests, two of them were performed at $R_\epsilon = -1$ (Cycle I and Cycle II) while the other was tested at $R_\epsilon \neq -1$ (Cycle III), and a stress-controlled test performed at $R = -0.66$. R_ϵ is related to the strain-controlled tests, and it indicates the ratio between the minimum and the maximum imposed total strain during the test. R is related to the stress-controlled test, and it is defined by the ratio between the minimum and the maximum imposed axial stress during the test. The experimental stabilized cycles were extracted from strain-controlled tests. Cycle II and Cycle III were used to calculate the values of C_3 , whereas Cycle I and Cycle II were employed to compute the values of C_1 , C_2 , γ_1 , σ_L , C_4 and γ_4 . And finally, the stress-controlled test allowed to calculate the value of γ_2 . In Fig. 2(a) the ability of the parameter C_3 to reproduce the mean point of the stabilized cycles is shown, while in Fig. 2(b) the comparisons between the experimental stabilized cycles of the strain-controlled tests performed at $R_\epsilon = -1$ and their corresponding modelled curves are reported. For brevity, only the modelled stabilized cycles of the strain-controlled tests are presented in this study given that the critical plane multiaxial fatigue criteria generally require to achieve a good prediction of the global properties of the stabilized cycles rather than the transient cycling. Nevertheless in Ref. [48] the ability of the used procedure to well reproduce the transient of the stress-controlled test was also verified. The numerical values of the CKH model parameters, which were used to model the constitutive behaviour of the material during the FE simulations of this research, are reported in Table 1.

Table 1

Numerical values of the parameters for CKH model with four backstress components.

Material	σ_L (MPa)	C_1 (MPa)	γ_1 —	C_2 (MPa)	γ_2 —	C_3 (MPa)	γ_3 —	C_4 (MPa)	γ_4
42CrMo4+QT	240	69.21×10^3	426	2.836×10^3	4.63	2.669×10^3	0	381.8×10^3	5000

**Figure 2:** (a) C_3 and $\chi_{3,0}$ to predict the mean point of the stabilized cycles of the strain-controlled tests, (b) comparisons between the experimental and the simulated stabilized cycles of the strain-controlled tests performed at $R_\varepsilon = -1$.**Table 2**

Significant parameters of the shots engaged in the shot-peening process.

Material	Intensity (N)	coverage	diameter (mm)	speed (m/s)
quenched steel	12.7	100%	0.25 ± 0.05	55 ± 5

2.3. Experimental quantities of the shot-peening process

The relevant quantities regarding the S70H shots and the principal parameters of the shot-peening process are reported in Table 2. The shots were propelled perpendicularly to the surface of the samples at the notch tip.

To measure the residual stresses, XRD measurements were carried out with the $\sin^2\psi$ technique and the modified χ method, which are described in [76]. A chrome anode was used, probing the lattice spacing of $\{211\}$ planes. The graphic explanations of the geometrical setup and the technological processes, performed before starting the measurements, are reported in Fig. 3. The component was subjected to a material removal by conventional milling, and then the electrochemical machining provided a step-by-step localized penetration in the zone where the residual stresses were measured. The measurements were extracted at three different points on the notch bisector of the specimens, and the distances of these three points from the notch tip are indicated in Table 3 and Table 4. The uncertainty referred to the values of the distances d_i from the notch tip is related to the penetration of the X-ray. The diameter of the spot was equal to $D = 1$ mm, the angle χ was varied from -40° to 40° with an oscillation of $\pm 5^\circ$ during the measurements, and the diffraction angle at zero residual stresses was $2\theta = 156^\circ$, provided that the anode was in chromium and the target material is ferritic steel. The configuration presented in Fig. 3(a) allowed one to measure the circumferential residual stresses, and a rotation of $\varphi = 90^\circ$ allowed one to measure the axial residual stresses. The measurements were carried out by Peen Serice S.r.l. The values of the axial $\sigma_{zz, \text{res}}$ and circumferential $\sigma_{\theta\theta, \text{res}}$ residual stresses measured at the end of the shot-peening process on the C-notched specimen, the plain specimen and the V-notched specimen are reported in Table 3. Unfortunately, it was not possible to extract reliable measurements for the initial residual stresses $\sigma_{zz, \text{res}}$ on the V-notched specimen, so only the initial residual stresses $\sigma_{\theta\theta, \text{res}}$ are reported in Table 3. As concerns the axial residual stresses at the end of the fatigue loading $\sigma_{zz, \text{res, ro}}$ and $\sigma_{\theta\theta, \text{res, ro}}$, they were only measured on a run-out sample

Table 3

Measured initial residual stresses for the plain specimen, for the C-notched specimen and for the V-notched specimen.

Specimen	$\sigma_{zz,res}$ (MPa)			$\sigma_{\theta\theta,res}$ (MPa)		
	$d_1 = 5 \pm 5$ μm	$d_2 = 50 \pm 5$ μm	$d_3 = 105 \pm 5$ μm	$d_1 = 5 \pm 5$ μm	$d_2 = 50 \pm 5$ μm	$d_3 = 105 \pm 5$ μm
Plain specimen	-367.5	-266	-83	-417	-370.5	-221
C-notched specimen	-427.5	-320.5	-233	-413	-359	-269.5
V-notched specimen	-	-	-	-382	-234	-155

Table 4

Measured residual stresses for the C-notched run-out specimen.

Specimen	$\sigma_{zz,res,ro}$ (MPa)			$\sigma_{\theta\theta,res,ro}$ (MPa)		
	$d_1 = 5 \pm 5$ μm	$d_2 = 55 \pm 5$ μm	$d_3 = 105 \pm 5$ μm	$d_1 = 5 \pm 5$ μm	$d_2 = 55 \pm 5$ μm	$d_3 = 105 \pm 5$ μm
C-notched specimen	-263	-122	-69	-309	-166	-65

and only regarding the C-notched specimen loaded at $R = -1$. The residual stresses measured on the run-out sample were indicated as the average stress of the final stabilized cycle. These last measurements are reported in Table 4.

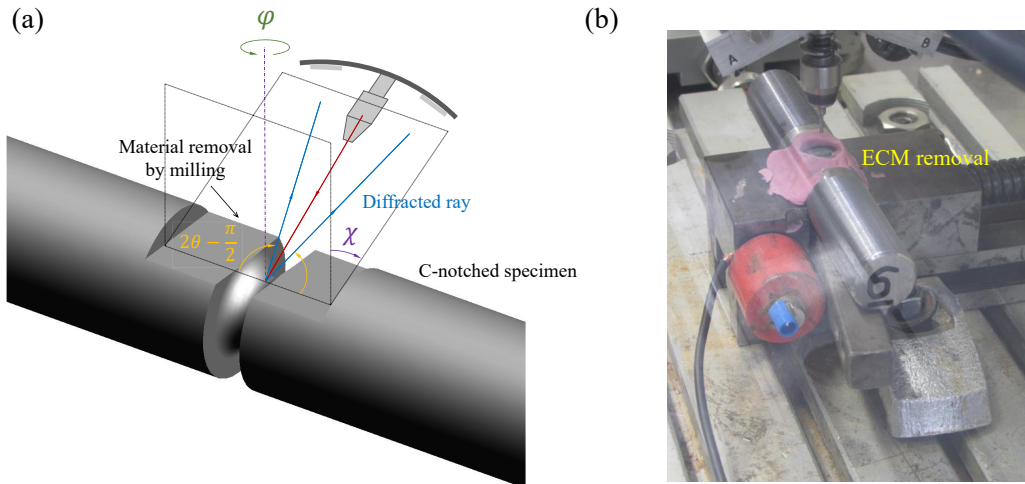


Figure 3: (a) Significant angles of the XRD measurement with $\sin^2\psi$ technique and the modified χ method, (b) XRD instrument to perform the residual stress measurements.

2.4. Experimental results of the calibrating specimens

The samples involved in this work were all uniaxially loaded. The experimental fatigue strength data, varying with the number of cycles, of the plain specimen and the V-notched specimen are reported in Fig. 4 and in Fig. 5. A linear fitting function was introduced to interpolate the experimental data of the fatigue strength. The nominal values of the ratio between the minimum and the maximum uniaxial stress during the loading were $R = -1$, $R = 0$, $R = 0.3$ and $R = 0.5$. The values of the V-notched specimen load ratios were referred to the minimum nominal net values of the stress and the maximum nominal net values of the stress. Given the high severity of the V-notch, the zone near the stress raiser underwent plasticity during the fatigue loading and therefore the values of R changed point by point during the tests except for the loading at $R = -1$.

In Table 5 the fatigue limits values of the V-notched specimen and the plain specimen, calculated through the linear fitting and for the different values of R involved in this study, are reported, and the fatigue limit was fixed at 10^7 cycles.

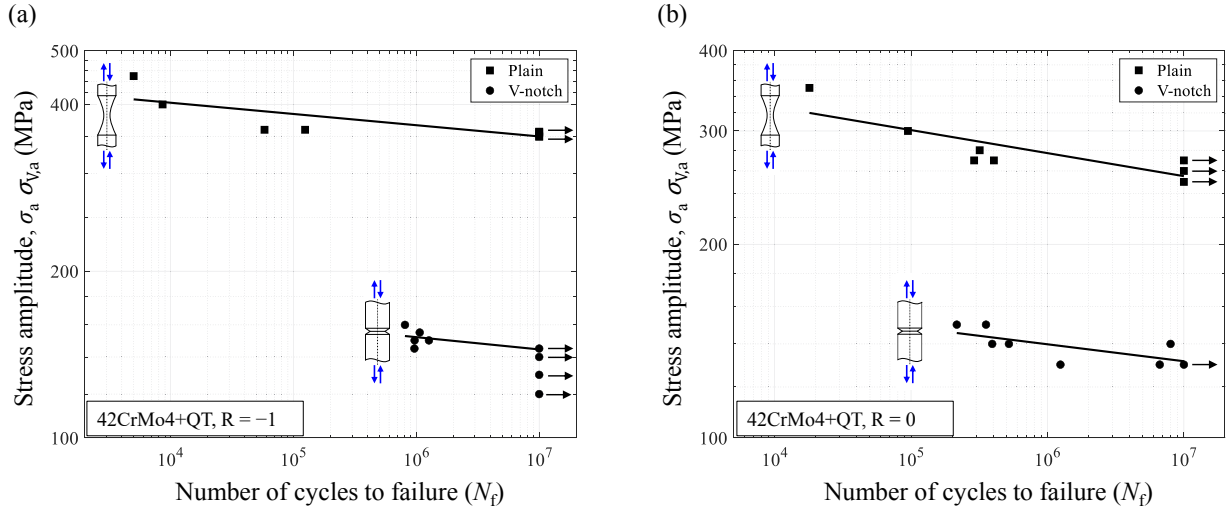


Figure 4: Steel 42CrMo4+QT fatigue tests, plain and V-notched specimens under axial loadings performed at (a) $R = -1$ and (b) $R = 0$

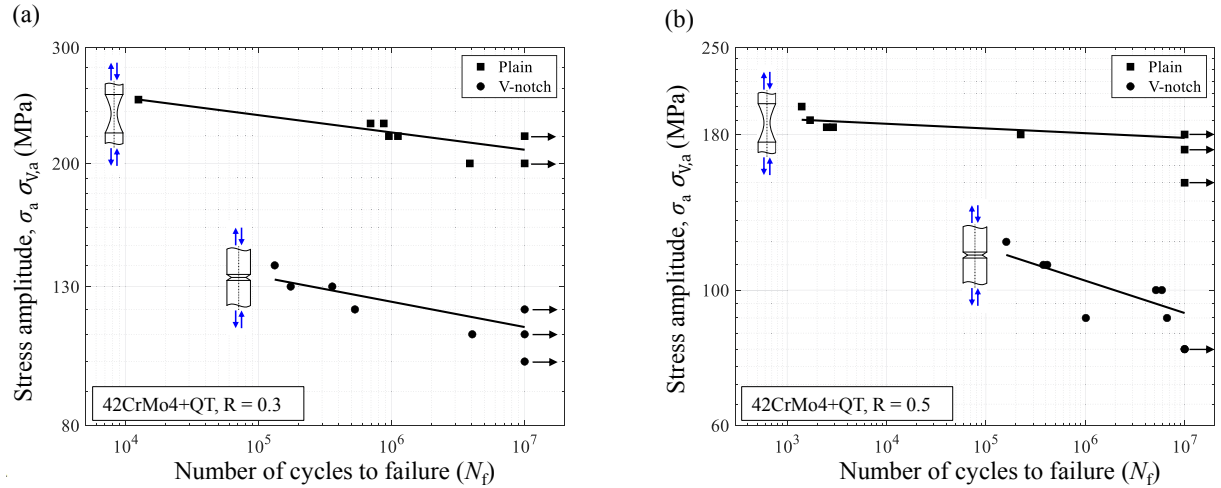


Figure 5: Steel 42CrMo4+QT fatigue tests, plain and V-notched specimens under axial loadings performed at (a) $R = 0.3$ and (b) $R = 0.5$

Table 5

Fatigue limits under mode I (axial) for the various nominal values of R and for the V-notched specimen and for the plain specimen.

	$R = -1$	$R = 0$	$R = 0.3$	$R = 0.5$
$\sigma_{V,a,fl}$ (MPa)	145	132	113	92
$\sigma_{a,fl}$ (MPa)	350	255	210	178

3. Reproduction of the measured residual stresses

3.1. Reproduction of the initial residual stresses

The reproduction of the initial residual stresses of the C-notched specimen followed the scheme presented in Fig. 6. A part of the specimen near the notch was selected to reproduce the residual stresses, and the distance of the point O' from the notch bisector was set as half of the notch radius. This last assumption is motivated by the fact that the effect of the shot-peening on the stress along the notch bisector becomes negligible after a certain distance. Given that the experimental values of the initial residual stresses $\sigma_{zz,res}$ and $\sigma_{\theta\theta,res}$ were available in three points of the notch bisector,

three slices of area were then reproduced. The width of each slice was set equal to $50 \mu\text{m}$, and the distances of the three points from the notch tip were $d_1 = 5 \pm 5 \mu\text{m}$, $d_2 = 55 \pm 5 \mu\text{m}$ and $d_3 = 105 \pm 5 \mu\text{m}$. In Fig. 6 the effect of the applied eigenstrains on an undeformed cube is represented, though it refers to the deformation that the cube would have if it was unconstrained. The value of α_{rr} was assumed null, given that the residual stresses $\sigma_{rr,\text{res}}$ were not measured and their effect was considered negligible. The cube of Fig. 6 was represented with an only bulk deformation given that the chosen frame of reference was principal for both the stress tensor and the strain tensor. To reproduce the initial residual

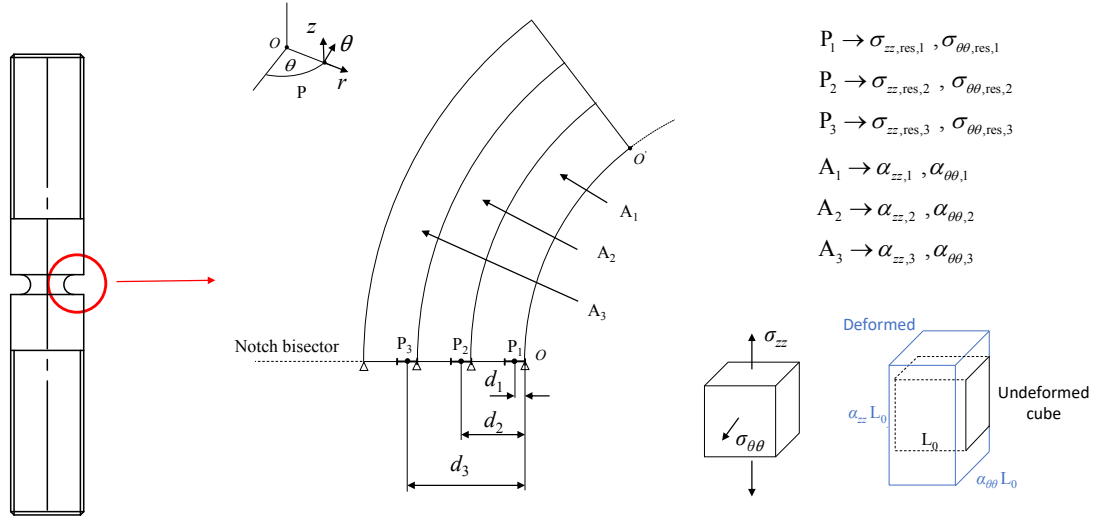


Figure 6: Geometric set-up and meaningful quantities to reproduce the initial residual stresses of the C-notched specimen.

stresses the stiffness matrix \mathbf{K} , which relates the residual stresses with the eigenstrains, was introduced. It is important to underline that the values of the residual stresses were referred to the individual nodes, whereas the eigenstrains were imposed as properties related to areas given that they were passed to the FE software through coefficients of thermal expansion as in Refs. [62, 67]. The vector $\{\sigma_{\text{res}}\}$ gathered the initial residual stresses in the Points P_1 , P_2 and P_3 , so we defined $\{\sigma_{\text{res}}\} = \{\sigma_{zz,\text{res},1} \sigma_{zz,\text{res},2} \sigma_{zz,\text{res},3} \sigma_{\theta\theta,\text{res},1} \sigma_{\theta\theta,\text{res},2} \sigma_{\theta\theta,\text{res},3}\}^t$. The vector $\{\alpha\}$ regrouped the values of the eigenstrains for each area A_1 , A_2 , A_3 so we defined $\{\alpha\} = \{\alpha_{zz,1} \alpha_{zz,2} \alpha_{zz,3} \alpha_{\theta\theta,1} \alpha_{\theta\theta,2} \alpha_{\theta\theta,3}\}^t$. The values of α_{zz} and $\alpha_{\theta\theta}$ regarding the non-shot-peened areas were automatically imposed null. To populate the first column of the matrix \mathbf{K} the value of $\alpha_{zz,1}$ was set equal to $1 \mu\epsilon/^\circ\text{C}$ while all the other components of the vector $\{\alpha\}$ were imposed as null, and an uniform temperature change of $\Delta T = 1^\circ\text{C}$ was given to all the areas. This last statement is explained in Fig. 7. A simulation with FE software was then performed, and the only load on the specimen was represented by the combination between the imposed temperature change and the nonzero value of the vector $\{\alpha\}$. At the end of the simulation the values of all the components of the vector $\{\sigma_{\text{res}}\}$ were extracted from the points P_1 , P_2 and P_3 and they represented the first column of the matrix \mathbf{K} . This iterative technique was implemented six times following the way mentioned above, for example during the second iteration the only nonzero imposed value of the vector $\{\alpha\}$ was $\alpha_{zz,2}$. To find the correct values of the eigenstrains to reproduce the initial residual stresses the linear system in eq. (2) was then solved.

$$\{\sigma_{\text{res}}\} = \mathbf{K} \{\alpha\} \quad (2)$$

The strategy to reproduce the initial residual stresses of the plain specimen followed the same principles of that proposed for the C-notched specimen, but the geometric set-up was different, as shown in Fig. 8. A rectangular was used to provide the geometric representation of the shot peened zone. The values of the length d'_1 , d'_2 and d'_3 were the same of those of the C-notched specimen d_1 , d_2 and d_3 . To reproduce the initial residual stresses of the V-notched specimen the principle behind the geometric representation was the same of that employed for the C-notched specimen. However, the measurements of the initial residual stresses $\sigma_{\theta\theta,\text{res}}$ could only be used given that those of $\sigma_{zz,\text{res}}$ were not available. To accomplish this identification the size of the matrix \mathbf{K} was 3×3 instead of 6×6 as it was for the

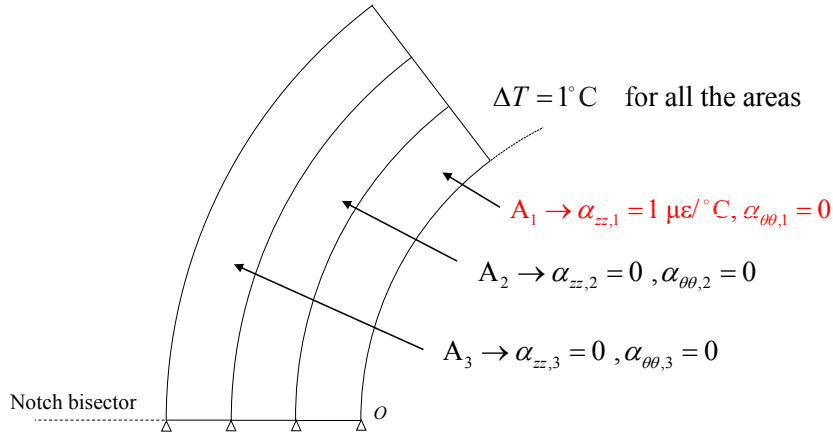


Figure 7: Imposed eigenstrains during the step to populate the first column of the matrix \mathbf{K} as concerns the reproduction of the initial residual stress of the C-notched specimen.

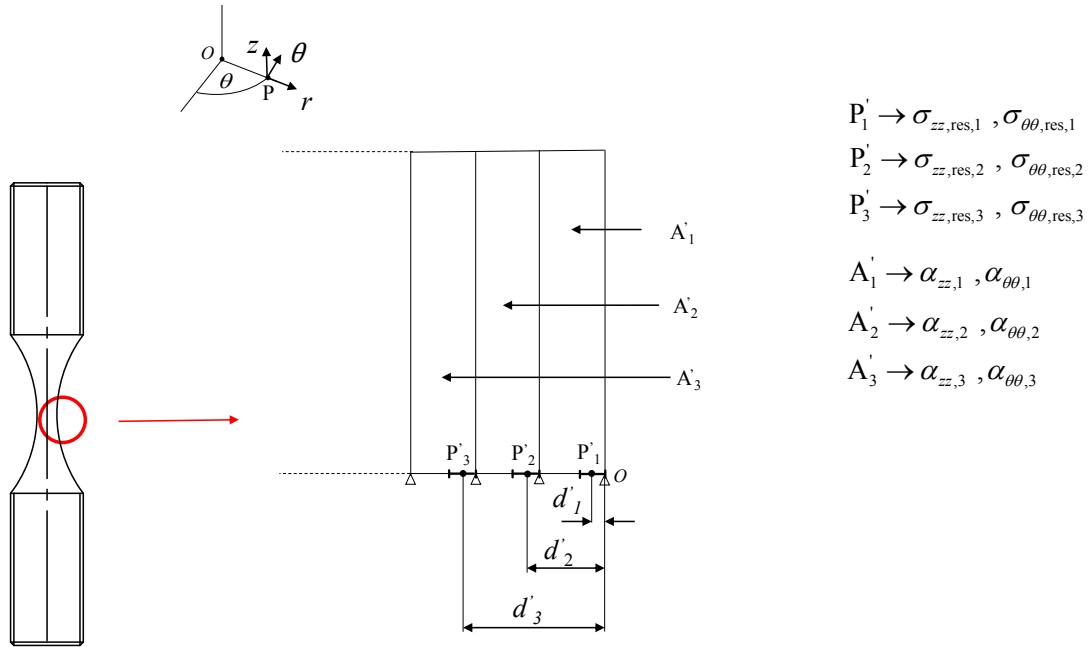


Figure 8: Geometric set-up and meaningful quantities to reproduce the initial residual stresses of the plain specimen.

C-notched specimen and for the plain specimen. To populate the matrix \mathbf{K} as concerns the V-notched specimen, a different strategy from that employed for the C-notched specimen and for the plain specimen was employed. To obtain the first column of the matrix, a FE simulation was performed considering $\alpha_{\theta\theta,1} = 1 \mu\epsilon/^\circ\text{C}$ and the corresponding value of $\alpha_{zz,1}$ given by the ratio between the calculated values of $\alpha_{zz,1}$ and $\alpha_{\theta\theta,1}$ of the C-notched specimen; the other components of the vector $\{\alpha\}$ were set as null. At the end of the simulation the values of $\sigma_{\theta\theta,res}$ were extracted from the three points P_1 , P_2 and P_3 , and they constituted the first column of the matrix. The same strategy was repeated for the second and the third column of the matrix \mathbf{K} . The assumption of having the same ratio for the V-notched specimen and the C-notched one was motivated by the similarity, given by the notch, between the two samples. Once the definitive values of $\alpha_{\theta\theta,1}$, $\alpha_{\theta\theta,2}$ and $\alpha_{\theta\theta,3}$ were determined for the V-notched specimen, the values of $\alpha_{yy,1}$, $\alpha_{yy,2}$, $\alpha_{yy,3}$ were then automatically determined. For example and for brevity, only the results of the reproduction of $\{\sigma_{res}\}$ as concern the C-notched specimen are reported in Fig. 9(b) for $\sigma_{zz,res}$ and in Fig. 9(c) for $\sigma_{\theta\theta,res}$. In Fig. 9(a) a portion of the nodal solution of $\sigma_{zz,res}$ obtained for the C-notched specimen in the reproduction of the initial residual stresses is reported.

It is important to highlight that during the reproduction and the validation of the initial residual stresses we assume a linear elastic behaviour of the material, but we remarked in the introduction that the CKH model was employed to model the cyclic plastic behaviour of the material. This aspect will be clarified in Section 3.2.

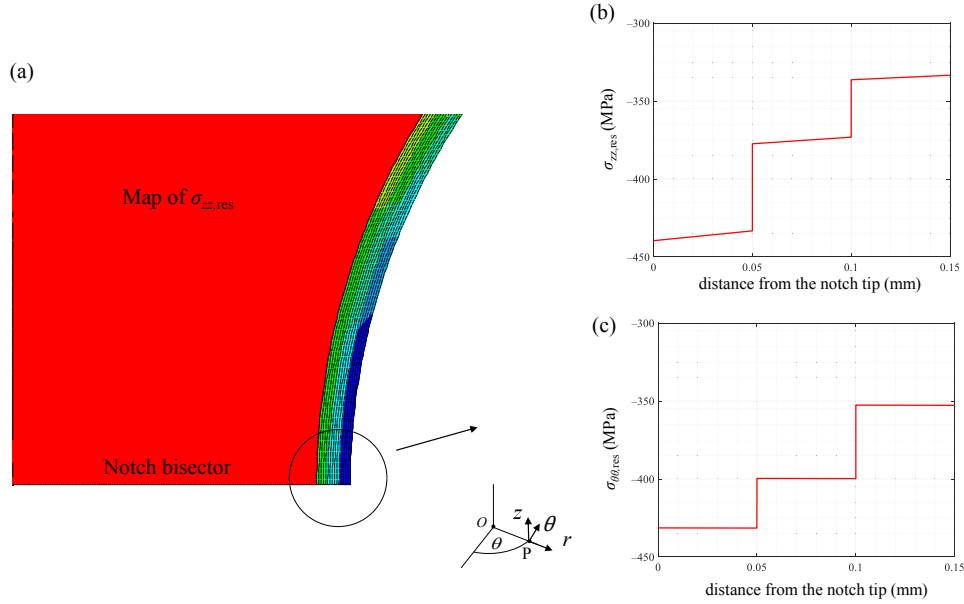


Figure 9: Reproduction of the initial residual stresses of the C-notched specimen: (a) map of the nodal solution regarding $\sigma_{zz,res}$, (b) trend of $\sigma_{zz,res}$ on the notch bisector, (C) trend of $\sigma_{\theta\theta,res}$ on the notch bisector.

3.2. Reproduction of the residual stresses measured at the end of the loading

Once the values of the eigenstrains were computed, the experimental initial residual stresses were reproduced. However, after setting the obtained values of the eigenstrains and carrying on the FE elastic-plastic simulations on the considered components, the material underwent a full relaxation, as shown in Fig. 10(a), and this was not in agreement with the experimental data which highlighted nonzero values of the measured residual stresses on the run-out specimen. The residual stresses obtained at the end of the fatigue loadings were modelled as the average stress of the stabilized cycle and so $\sigma_{zz,res,ro} = (\sigma_{zz}^{max,stab} + \sigma_{zz}^{min,stab})/2$, where $\sigma_{zz}^{max,stab}$ and $\sigma_{zz}^{min,stab}$ are respectively the maximum and minimum value of the stress of the stabilized cycle. It was noted that a value of the elastic limit σ_L resulting into an elastic-plastic shakedown, with a nonzero value of the hysteresis area, always produces a full relaxation of the material for the C-notched specimen even loaded at $R = -1$. The problem was to find the adequate values of the elastic limit for the areas A_1 , A_2 and A_3 to replicate the measured values of the final residual stresses. The idea was to put the material into the condition to not fully relax in the shot-peened zone as shown in Fig. 10(b), but this condition can only be reached with a considerable increase of the value of the elastic limit. According to the research mentioned in the introduction, as for example [49, 50, 51, 52], an increase of hardness of the shot peened zone with respect to the base material was observed. Given this evidence from the literature, in this study a correlation between an increase of hardness and an increase of the elastic limit of the shot-peened zone was supposed, and this is the main point behind the procedure adopted to replicate the residual stresses measured after the fatigue loading. The axial residual stresses of the run-out C-notched specimen, loaded at $R = -1$, were used to establish the values of the elastic limit at the notch subsurface zones. The obtained elastic limits were then extended to the V-notched and the plain specimens for the other values of R . The procedure to compute the values of $\{\sigma_L(A_i)\} = \{\sigma_L(A_1) \sigma_L(A_2) \sigma_L(A_3)\}^t$ to reproduce the measured residual stresses of the C-notched run-out specimen is presented in Fig. 11. The geometric set-up was the same as that proposed during the reproduction of the initial residual stresses of the C-notched specimen. The procedure started setting the distribution of eigenstrains found in Section 3.1 and this was the first loadstep of the loading. After this, an iteration matrix \mathbf{J} was introduced and several FE simulations were performed to populate the matrix. In the first simulation the elastic limit was set equal to that of the base material $\sigma_L = 240\text{MPa}$ for all the three areas A_1 , A_2 and A_3 and the resulting $\sigma - \epsilon$ trend, registered in P_1 , is shown in Fig. 10(a) where the maximum and the minimum

Elastic-plastic TCD with shot peening residual stresses

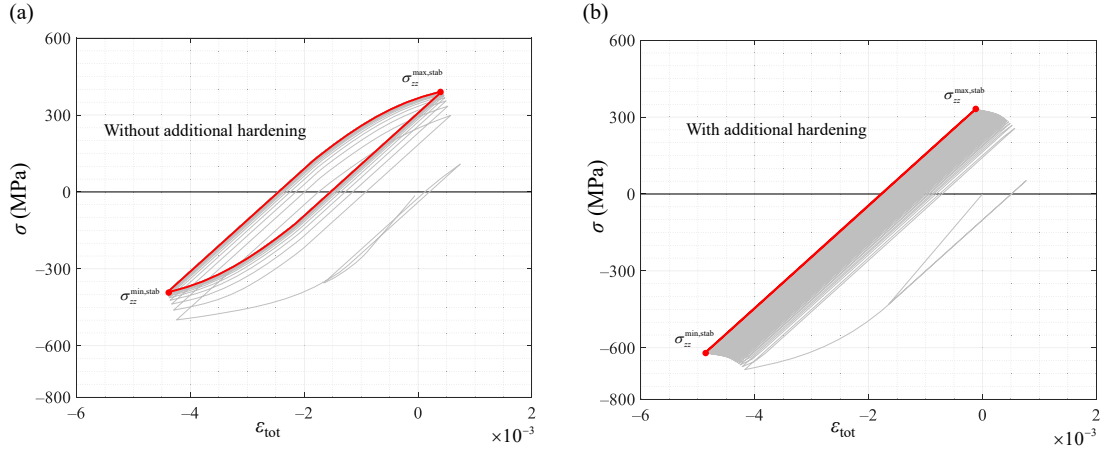


Figure 10: Elastic-plastic behaviour of the material in point P_1 for the C-notched specimen loaded at $R = -1$: (a) considering the nominal value of σ_L , (b) considering a higher value of σ_L .

values of the stress of the stabilized cycle are almost opposite. The average stresses of the stabilized cycles, extracted from the points P_1 , P_2 and P_3 , were then computed at the end of the simulation. The other simulations were performed considering an increased value of the elastic limit only for the areas A_1 , A_2 and A_3 , while the rest of the material maintained the value of the elastic limit of the base material. This assumption is related to the very local effect of shot peening in terms of hardening increase. To determine the first column of the matrix \mathbf{J} , the simulation was executed considering $\sigma_L(A_1) = \sigma_L + \Delta\sigma_L$ and $\sigma_L(A_2) = \sigma_L(A_3) = \sigma_L$. At the end of the simulation, the average stress of the stabilized cycles extracted from points P_1 , P_2 and P_3 was calculated and the $\sigma - \epsilon$ trend regarding the point P_1 is reported in Fig. 10(b) showing that the cycle results in a negative value of the average stress for the stabilized cycle. It is worth noting that, an increase of σ_L introduces a zero hysteresis area, at least locally, that in turn avoids the relaxation which otherwise would have produced a quick decay of the beneficial compressive residual stresses induced by the shot peening. The mathematical formalization of the first column of the matrix \mathbf{J} is reported in eq. (3) where each line was computed through the ratio between $\Delta\sigma_{zz,res,ro}(P_n)$ and $\Delta\sigma_L$. The numerator was represented by the increase of the average stress of the stabilized cycle obtained in point P_n after an increase of the value of the elastic limit, whereas the denominator was represented by the increased imposed value of the elastic-limit.

$$\mathbf{J}_{(1:3,1)} = \begin{pmatrix} \frac{\Delta\sigma_{zz,res,ro}(P_1)}{\Delta\sigma_L} \\ \frac{\Delta\sigma_{zz,res,ro}(P_2)}{\Delta\sigma_L} \\ \frac{\Delta\sigma_{zz,res,ro}(P_3)}{\Delta\sigma_L} \end{pmatrix} \quad (3)$$

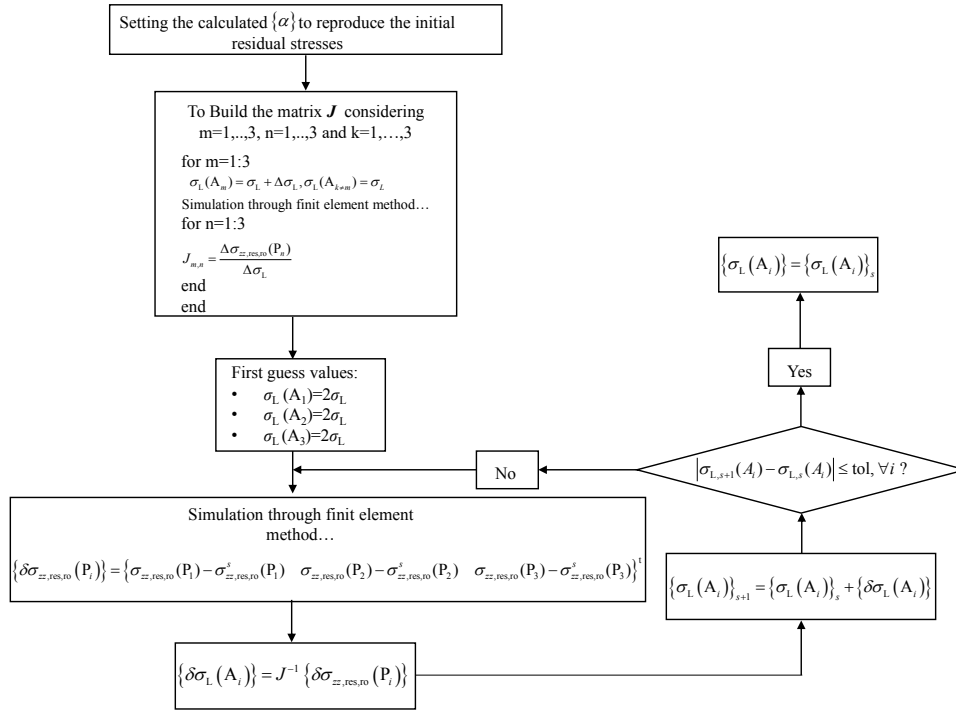
This procedure was repeated two more times with the same increment of the elastic limit $\Delta\sigma_L$, for example during the second iteration we imposed that $\sigma_L(A_2) = \sigma_L + \Delta\sigma_L$ and $\sigma_L(A_1) = \sigma_L(A_3) = \sigma_L$. The choice of the value of $\Delta\sigma_L$ was not immediate and in this study the utilized value was set equal to $\Delta\sigma_L = \sigma_L$. The chosen value of $\Delta\sigma_L$ allowed to avoid a full relaxation. Once the matrix \mathbf{J} was built, the iterative technique started and the first guess values were set as $\sigma_L(A_1) = \sigma_L(A_2) = \sigma_L(A_3) = 2\sigma_L$. A first FE simulation was performed until the values of $\sigma_{zz}^{max,stab}$ and $\sigma_{zz}^{min,stab}$ were reached. At the end of this simulation it was possible to compute the vector $\{\delta\sigma_{zz,res,ro}(P_i)\} = \left\{ \sigma_{zz,res,ro}(P_1) - \sigma_{zz,res,ro}^s(P_1) \quad \sigma_{zz,res,ro}(P_2) - \sigma_{zz,res,ro}^s(P_2) \quad \sigma_{zz,res,ro}(P_3) - \sigma_{zz,res,ro}^s(P_3) \right\}^t$ related to the error between the experimental values of the residual stresses and those obtained from the FE simulation. The evaluation $\{\delta\sigma_L(A_i)\} = \mathbf{J}^{-1} \{\delta\sigma_{zz,res,ro}(P_i)\}$, inspired by the Newton-Raphson methodology, allowed to find the increment of $\{\sigma_L(A_i)\}$ to be imposed in order to approach the desired values of the residual stresses, and the updated values of the components of $\{\sigma_L(A_i)\}$ were then employed in a further FE simulation. The procedure was repeated until the difference between each of the components of the vector $\{\sigma_L(A_i)\}$ calculated at the step $s + 1$ and those calculated at the step s was lower or equal than a chosen small tolerance. Once the vector $\{\sigma_L(A_i)\}$ was

Table 6

Obtained values of σ_L to reproduce the axial residual stresses measured after the fatigue loading and comparisons between the experimental values and the modelled values of the residual stresses.

	Pred. σ_L (MPa)	Pred. $\sigma_{zz,res,ro}$ (MPa)	Exp. $\sigma_{zz,res,ro}$ (MPa)	Pred. $\sigma_{\theta\theta,res,ro}$ (MPa)	Exp. $\sigma_{\theta\theta,res,ro}$ (MPa)
$d_1 = 5 \pm 5 \mu\text{m}$	482.3	-262.5	-263	-326	-309
$d_2 = 55 \pm 5 \mu\text{m}$	409.1	-122.2	-122	-168	-166
$d_3 = 105 \pm 5 \mu\text{m}$	390.1	-67.0	-69	-95	-65

found, the hypothesis about the linear elastic behaviour of the material during the reproduction of the initial residual stresses had to be verified. In Table 6 the calculated values of σ_L to replicate the residual stresses measured at the end of the loading are reported. All the values of the measured initial residual stresses reported in Table 3 are sufficiently smaller than the obtained values of σ_L at the examined distances from the notch tip. This confirmed that the original assumption about supposing a linear elastic behaviour of the material, to reproduce the initial residual stresses, was in fact correct, given that the material was supposed to undergo a considerable local hardening after the shot peening. It is important to remark that in the shot peened zone the elastic limit σ_L was the only parameter of the CKH model which changed with respect to the parameters of the base material presented in 2.2 otherwise other information would have been required and a more complex calculation would have resulted.

**Figure 11:** Procedure to reproduce the residual stresses measured after the fatigue loading.

4. Application of the TCD combined with the SWT multiaxial fatigue criterion

Once the initial residual stresses (just after the shot peening) and the final residual stresses (after the fatigue run out) were successfully reproduced, the fatigue strength predictions regarding the C-notched specimen were carried out, using the combination of a multiaxial fatigue criterion and the LM. The calibrations of the constants of the fatigue model were carried out on the shot peened samples and not on the unpeened specimens. This because the fatigue endurance and the elastic limit might be correlated as also stated by Paul in Ref. [77]. The SWT multiaxial fatigue

Table 7

Values of the critical distances and of the constants of SWT criterion calculated at the fatigue limit and for the various values of R .

	$R = -1$	$R = 0$	$R = 0.3$	$R = 0.5$
L_{SWT} (mm)	0.056	0.046	0.244	0.188
a_{SWT} (MPa)	0.722	1.27	0.718	0.732

criterion was assumed an effective model in this situation where the fatigue loading is just mode I and the mean stress is quite high. This criterion is defined by the expression presented in eq. (4) where ϵ_a and σ_n^{\max} are the alternating component of the normal strain and the maximum normal stress respectively, and they are both computed on the SWT critical plane. This critical plane is that of maximum normal strain amplitude. The normal strain amplitude computed in the SWT criterion includes both the elastic and the plastic components of the total strain.

$$\epsilon_a \sigma_n^{\max} = a_{\text{SWT}} (N_f) \quad (4)$$

In this study the specimens were uniaxially loaded, and despite the notch, which resulted in a multiaxial state of stress, and the presence of the residual stresses, the critical plane was that perpendicular to the axis of the specimen. According to the Figs. 6 and 8 the normal to the critical plane was defined by the axis z , so the quantities involved in eq. (4) were σ_{zz}^{\max} and $\epsilon_{zz,a}$. These stress and strain components were extracted from the stabilized cycles obtained through the FE simulations. It is important to remark that the values of the eigenstrains, presented in Section 3.1, and the values of the elastic limit of the shot peened zone, exposed in 3.2, were set during the FEM simulations as material properties of the areas representing the shot peened zone. The stabilized cycle, as intended for the SWT criterion, was defined when σ_{zz}^{\max} and $\epsilon_{zz,a}$ did not change considerably from one cycle to another. This does not imply that the cycle has already reached a complete stabilization in terms of average strain, but that the global properties of the cycle involved in the SWT criterion do not change anymore. The SWT multiaxial fatigue criterion was employed together with the LM and in particular the V-notched specimen and the plain specimen were combined according to eq. (5) to find the unknown parameters, which were L_{SWT} and a_{SWT} . These last quantities were computed varying with the number of cycles and for the various values of R . The strategy about the combination of the LM together with the SWT multiaxial fatigue criterion is exposed in Fig. 12. The combination of the V-notched specimen and of the plain specimen to calculate the values of the critical distances was coherent with the proposal of Santus et. al. [6, 7], and it is based on the strategy of combining the lowest and the highest gradients for a robust determination of these parameters.

$$\int_0^{L_{\text{SWT}}} \epsilon_{V,a} \sigma_{n,V}^{\max} dr = \int_0^{L_{\text{SWT}}} \epsilon_{pl,a} \sigma_{n,pl}^{\max} dr \quad (5)$$

$$\frac{1}{2L_{\text{SWT}}} \int_0^{L_{\text{SWT}}} \epsilon_{V,a} \sigma_{n,V}^{\max} dr = a_{\text{SWT}}$$

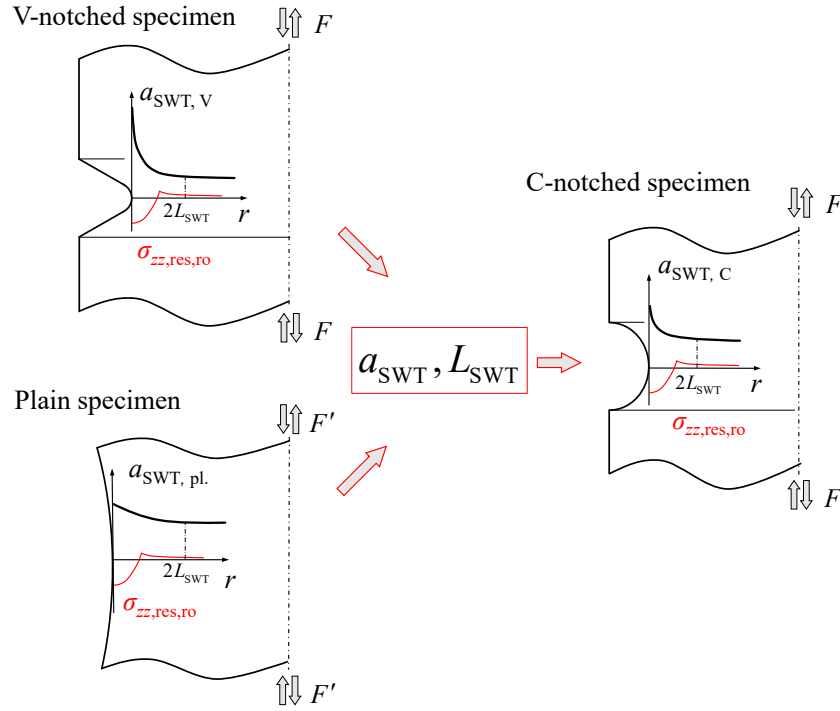
The values of L_{SWT} and a_{SWT} obtained at the fatigue limit and for the engaged values of R are reported in Table 7. Once the values of L_{SWT} and of a_{SWT} were calculated, the C-notched specimen was employed for validation according to eq. (6) and the comparisons between the experimental and the calculated fatigue limits are reported in Table 8.

$$\frac{1}{2L_{\text{SWT}}} \int_0^{L_{\text{SWT}}} \epsilon_{C,a} \sigma_{n,C}^{\max} dr = a_{\text{SWT}} \quad (6)$$

The obtained constants a_{SWT} reported in Table 7 are very similar even if there is a considerable difference regarding the value of a_{SWT} obtained at $R = 0$. The constant a_{SWT} in principle only depends on the number of cycles to failure and it should not depend on R . Given this last statement, a different way to apply the SWT multiaxial fatigue criterion combined with the LM was proposed. It employed a unique value of the critical distance only dependent on the number of cycles to failure just obtained as the average of the critical distances calculated at the same number of cycles and for the different values of R . Once the averaged critical distance was obtained, it was engaged to calculate the

Table 8Predicted fatigue limits for the C-notched specimen at the various values of R .

	Exp. $\sigma_{C,a,fl}$ (MPa)	Pred. $\sigma_{C,a,fl}$ (MPa)	Err. (%)
$R = -1$	275	287	4.2
$R = 0$	241	253	4.7
$R = 0.3$	200	182	-9.0
$R = 0.5$	169	156	-7.7

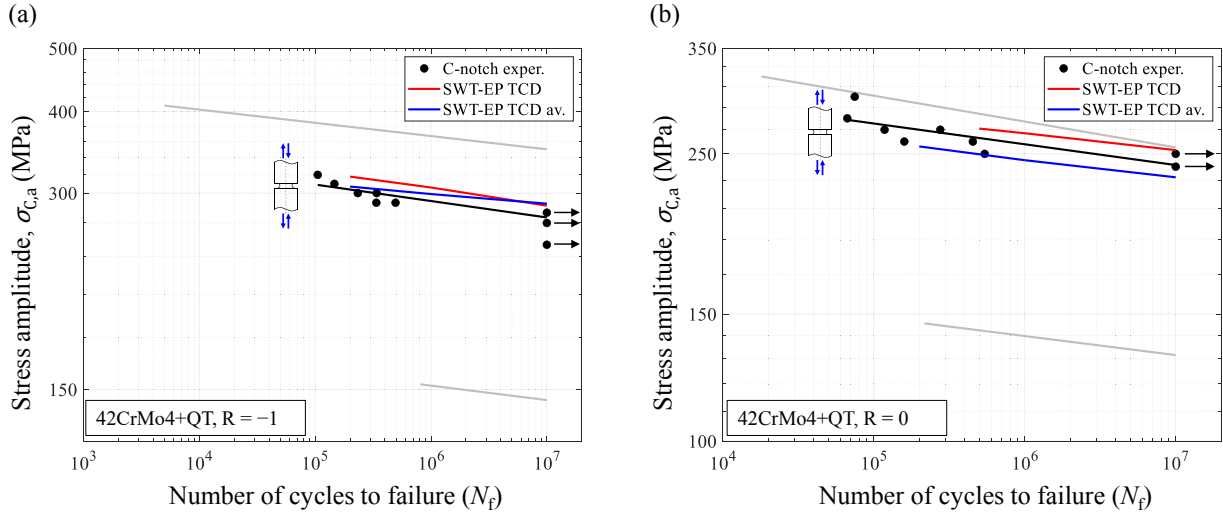
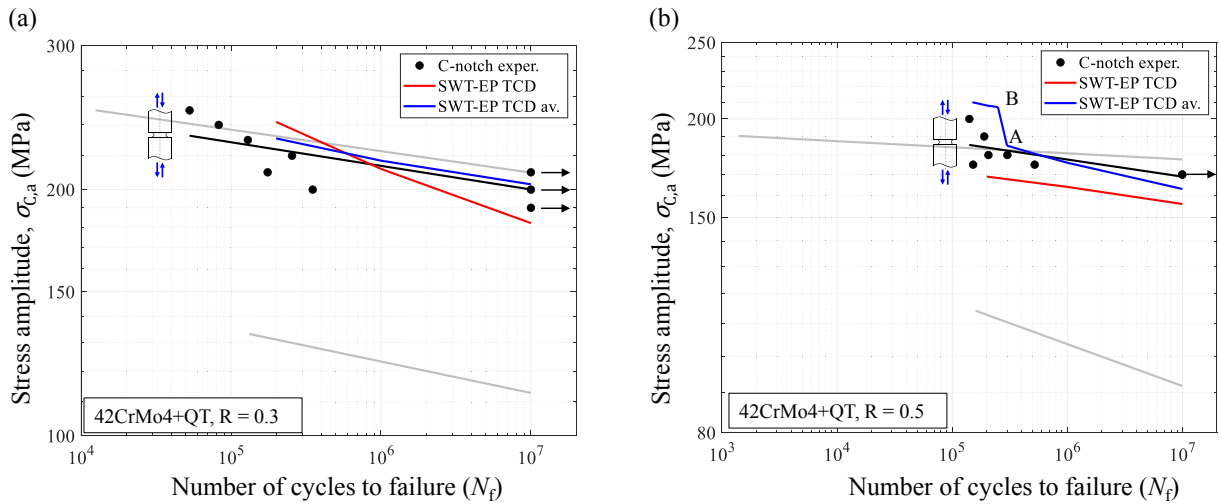
**Figure 12:** Procedure to calculate the critical distance and then provide a validation on the C-notched specimen.

corresponding constants a_{SWT} for the V-notched specimen and for the plain specimen at the different values of R . The obtained eight values of the constants (4 for the V-notched specimen and 4 for the plain specimen) were then averaged to obtain a unique value of the constant a_{SWT} . At the fatigue limit the obtained averaged value of the critical distance was $L_{SWT,av} = 0.134$ mm and the corresponding averaged value of the constant of the criterion was $a_{SWT,av} = 0.826$ MPa. This operation was repeated varying the number of cycles and the C-notched was considered for validation (i.e. assuming the role of the component to be designed). The results of this last procedure, just for the fatigue limit, are reported in Table 9, and quite small prediction errors are evident. In Figs. 13 the comparisons between the experimental data and the predicted fatigue strength curves are shown according to the SWT multiaxial fatigue criterion. The red curves represent the first approach proposed in this study regarding the combination of the LM with the SWT multiaxial fatigue criterion for each load ratio R taken separately. The blue curves are related to the second proposed approach, which involved the same values of the critical distance and of the constant a_{SWT} just dependent on the number of cycles to failure, and an accurate prediction was again obtained within the HCF investigated range.

In Fig. 14(b), it is worth noting that at 3×10^5 cycles there is a step of the blue line representing the predicted results using this latter averaged critical distance approach. This situation can be explained by focusing on the relaxation of the stress near the notch tip. In Fig. 15 two different situations are presented, both showing the $\sigma - \epsilon$ trend obtained at the same distance from the notch tip. In Fig. 15(a), referring to the loading point A of Fig. 14(b), the results are obtained by applying the predicted value of fatigue strength at 3×10^5 cycles, whereas Fig. 15(b), referring to the loading point B of Fig. 14(b), is obtained by the predicted value of the fatigue strength at 2.5×10^5 cycles. In Fig. 15(b)

Table 9Predicted fatigue limits for the C-notched specimen at the various values of R using the averaged critical distance.

	Exp. $\sigma_{C,a,fl}$ (MPa)	Pred. $\sigma_{C,a,fl}$ (MPa)	Err. (%)
$R = -1$	275	289	5.1
$R = 0$	241	232	-3.7
$R = 0.3$	200	203	1.5
$R = 0.5$	169	163	-3.5

**Figure 13:** Test results of C-notched specimen and curve predictions with the SWT multiaxial fatigue criterion (a) $R = -1$, (b) $R = 0$.**Figure 14:** Test results of C-notched specimen and curve predictions with the SWT multiaxial fatigue criterion (a) $R = 0.3$, (b) $R = 0.5$.

the stress undergoes a considerable relaxation while in Fig. 15(a) the stress undergoes a perfect elastic shakedown. The relaxation of the stress caused a decrease of the maximum stress reached, whereas a perfect elastic-shakedown keeps constant the maximum stress reached cycle per cycle. Given that the maximum stress of the stabilized cycle is a useful quantity for the SWT multiaxial fatigue criterion, the relaxation of the stress explains the need to move to higher values of the predicted $\sigma_{C,a}$ at number of cycles lower than 3×10^5 .

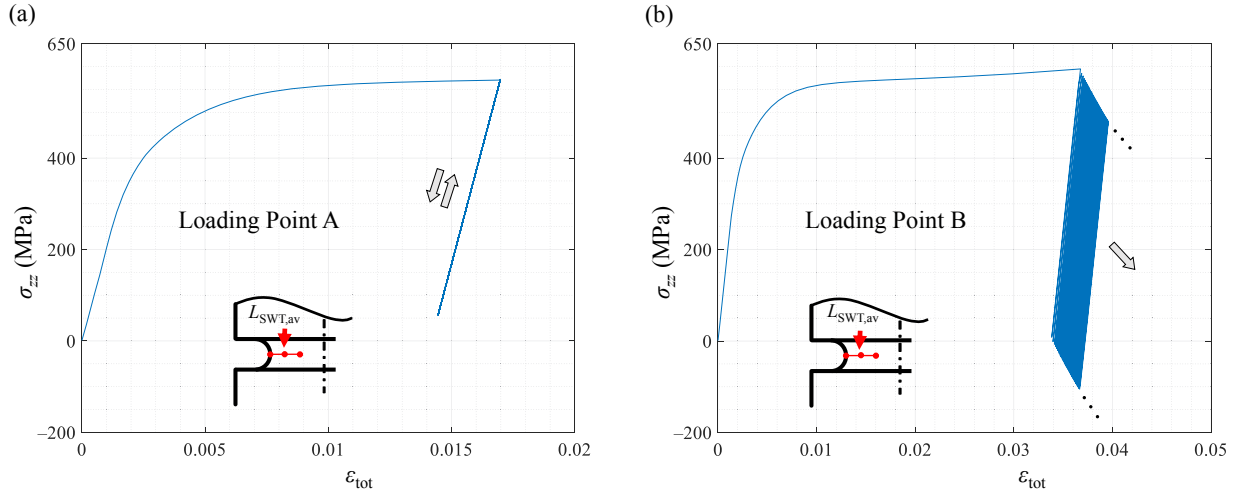


Figure 15: Stress and strain loading history obtained with the Chaboche model at the distance $L_{SWT,av}$ from the notch tip corresponding to 2×10^5 cycles (a) $\sigma_{C,a} = 182$ MPa (b) $\sigma_{C,a} = 210$ MPa.

5. Conclusions

This study investigated the uniaxial fatigue strength, for different values of the fatigue load ratio, of shot peened notched components made of 42CrMo4 quenched and tempered steel. The main conclusions are the following:

1. The CKH model was employed to properly represent the cyclic plastic behaviour of the material. This was certainly required, since otherwise with a purely elastic behaviour the maximum value of the stress reached at high values of the fatigue load ratio was much higher than the ultimate stress of the material.
2. The initial residual stresses, measured through the XRD $\sin^2\psi$ technique and the modified χ method, were reproduced similarly to the ERM technique. The only difference was that the ERM involves the superposition of triangular basis functions, whereas in this study the distribution of eigenstrains was realized through the superposition of rectangular basis functions. The used technique was linear and it provided an exact reproduction of the initial residual stresses.
3. The axial residual stresses measured at the end of the fatigue loading with the XRD $\sin^2\psi$ technique and the modified χ method on the C-notched specimen loaded at $R = -1$, were replicated considering a further hardening of the material due to the shot peening process. This hypothesis was supported considering a relationship between the increase of hardness of the shot peened zone and the increase of the elastic limit of the shot peened zone. The used strategy provided a nonlinear iterative technique to find the correct values of the elastic limit of the different subsurface zones below the shot peened surface. The values found of this modified elastic limits were then extended to the FE simulations of the other specimens loaded at different values of R . The achieved accuracy of the used technique is shown in Table 6 and the resulting errors are significantly low even for the values of the circumferential residual stresses $\sigma_{\theta\theta,res,ro}(P_i)$, which were used as validators of the proposed procedure. Generally when multiaxial fatigue criteria are applied to notched and shot peened samples, a purely elastic behaviour of the material is supposed and the measured residual stresses at the end of the fatigue loading are added to the meaningful quantities of the criteria using the superposition principle. In this study, multiaxial fatigue criteria quantities, obtained at the end of the FEM simulations, already include the effects of the residual stresses, and they can be directly introduced in the mathematical formalizations of the criteria. According to Fig. 10(b), the reproduction of the residual stresses measured at the end of the fatigue loading was obtained avoiding the material to fully relax, and this was achieved with an almost null value of the hysteresis area. According to these simulations, the shot peening treatment provided a residual compressive state of stress and an almost null value of the hysteresis area, and both these two components can be considered beneficial to the fatigue strength of the sample given that even the hysteresis area can be considered an increasing damage effect, since the strain amplitude would be increased.
4. The V-notched and the plain specimens were employed, according to the combination of the SWT multiaxial fatigue criterion and of the LM, to calculate the values of the critical distances and those of the constants of the

criterion at different numbers of cycles. This latter procedure was carried out in two different ways. According to the first approach, the values of the critical distances and of the constants of the SWT multiaxial fatigue criterion at the various nominal values of R were calculated, whereas the second considered a unique averaged value of the critical distance for all the values of R at a fixed number of cycles to obtain a unique value of the constant of the SWT multiaxial fatigue criterion. This other approach was developed considering that the constant of the SWT multiaxial fatigue criterion should not depend on the value of R , since the criterion already incorporates the maximum stress effect, but it only depends on the number of cycles. The C-notched specimen was then involved to validate the fatigue strength prediction. The calculated values of the fatigue limits are shown in Table 8, regarding the first proposed technique, and in Table 9, with the averaged critical distances. The predictive errors are in both cases below the 10%. The predicted fatigue strength curves for various numbers of cycles are reported in Fig. 13 and in Fig. 14 showing good prediction accuracy even at a numbers of cycles below the fatigue limit within the HCF regime.

CRediT authorship contribution statement

Ciro Santus: Methodology; Software; Validation; Data Curation; Writing- Reviewing and Editing. **Lorenzo Romanelli:** Methodology; Software; Validation; Data Curation; Writing- Reviewing and Editing. **Tommaso Grossi:** Methodology; Software; Validation; Data Curation; Writing- Reviewing and Editing. **Leonardo Bertini:** Methodology; Software; Validation; Data Curation; Writing- Reviewing and Editing. **Luca Le Bone:** Data curation; Resources; Supervision; Validation. **Francesco Chiesi:** Data curation; Resources; Supervision; Validation. **Leonardo Tognarelli:** Data curation; Resources; Supervision; Validation.

Declaration of Competing Interest

The authors declare that they have no known competing financial interests or personal relationships that could have appeared to influence the work reported in this paper.

Acknowledgements

The authors would like to thank Engineer Michele Bandini and Peen Service S.r.l. for performing the shot peening on the samples and for measuring the residual stresses.

References

- [1] H. Neuber, Theorie der technischen Formzahl, Forschung auf dem Gebiete des Ingenieurwesens 7 (6) (1936) 271–274. doi:10.1007/bf02584908.
- [2] H. Neuber, Theory of notch stresses : principles for exact calculation of strength with reference to structural form and material, 1958.
- [3] R. E. Peterson, Notch sensitivity, Metal fatigue (1959) 293–306.
- [4] D. Taylor, The Theory of Critical Distances, Elsevier Science, 2007.
- [5] M. H. E. Haddad, K. N. Smith, T. H. Topper, Fatigue crack propagation of short cracks, Journal of Engineering Materials and Technology 101 (1) (1979) 42–46. doi:10.1115/1.3443647.
- [6] C. Santus, D. Taylor, M. Benedetti, Determination of the fatigue critical distance according to the Line and the Point Methods with rounded V-notched specimen, International Journal of Fatigue 106 (2018) 208–218. doi:10.1016/j.ijfatigue.2017.10.002.
- [7] C. Santus, D. Taylor, M. Benedetti, Experimental determination and sensitivity analysis of the fatigue critical distance obtained with rounded V-notched specimens, International Journal of Fatigue 113 (2018) 113–125. doi:10.1016/j.ijfatigue.2018.03.037.
- [8] M. Benedetti, C. Santus, V. Fontanari, D. Lusuardi, F. Zanini, S. Carmignato, Plain and notch fatigue strength of thick-walled ductile cast iron EN-GJS-600-3: A double-notch critical distance approach to defect sensitivity, International Journal of Fatigue 152 (2021) 106414. doi:10.1016/j.ijfatigue.2021.106414.
- [9] L. Susmel, D. Taylor, A simplified approach to apply the theory of critical distances to notched components under torsional fatigue loading, International Journal of Fatigue 28 (4) (2006) 417–430. doi:https://doi.org/10.1016/j.ijfatigue.2005.07.035. URL <https://www.sciencedirect.com/science/article/pii/S0142112305002124>
- [10] L. Susmel, D. Taylor, The Theory of Critical Distances to estimate finite lifetime of notched components subjected to constant and variable amplitude torsional loading, Engineering Fracture Mechanics 98 (2013) 64–79. doi:10.1016/j.engfracmech.2012.12.007.
- [11] C. Santus, F. Berto, M. Pedranz, M. Benedetti, Mode III critical distance determination with optimized V-notched specimen under torsional fatigue and size effects on the inverse search probability distribution, International Journal of Fatigue 151 (2021) 106351. doi:10.1016/j.ijfatigue.2021.106351.
- [12] A. Carpinteri, A. Spagnoli, S. Vantadori, D. Viappiani, A multiaxial criterion for notch high-cycle fatigue using a critical-point method, Engineering Fracture Mechanics 75 (7) (2008) 1864–1874. doi:10.1016/j.engfracmech.2006.11.002.

- [13] T. Zhao, Y. Jiang, Fatigue of 7075-T651 aluminum alloy, *International Journal of Fatigue* 30 (5) (2008) 834–849. doi:10.1016/j.ijfatigue.2007.07.005.
- [14] Z.-R. Wu, X.-T. Hu, Y.-D. Song, Multiaxial fatigue life prediction for titanium alloy TC4 under proportional and nonproportional loading, *International Journal of Fatigue* 59 (2014) 170–175. doi:10.1016/j.ijfatigue.2013.08.028.
- [15] P. Lopez-Crespo, B. Moreno, A. Lopez-Moreno, J. Zapatero, Study of crack orientation and fatigue life prediction in biaxial fatigue with critical plane models, *Engineering Fracture Mechanics* 136 (2015) 115–130. doi:10.1016/j.engfracmech.2015.01.020.
- [16] L. Bertini, L. L. Bone, C. Santus, F. Chiesi, L. Tognarelli, High load ratio fatigue strength and mean stress evolution of quenched and tempered 42CrMo4 steel, *Journal of Materials Engineering and Performance* 26 (8) (2017) 3784–3793. doi:10.1007/s11665-017-2845-x.
- [17] S.-P. Zhu, Z.-Y. Yu, J. Correia, A. D. Jesus, F. Berto, Evaluation and comparison of critical plane criteria for multiaxial fatigue analysis of ductile and brittle materials, *International Journal of Fatigue* 112 (2018) 279–288. doi:10.1016/j.ijfatigue.2018.03.028.
- [18] M. A. Meggiolaro, J. T. P. de Castro, A deviatoric tensile-based critical plane model to predict peak/mean normal stress effects in multiaxial fatigue, *International Journal of Fatigue* 155 (2022) 106615. doi:10.1016/j.ijfatigue.2021.106615.
- [19] R. Branco, J. D. Costa, P. A. Prates, F. Berto, C. Pereira, A. Mateus, Load sequence effects and cyclic deformation behaviour of 7075-T651 aluminium alloy, *International Journal of Fatigue* 155 (2022) 106593. doi:10.1016/j.ijfatigue.2021.106593.
- [20] R. Branco, J. D. Costa, L. P. Borrego, F. Berto, S. M. J. Razavi, W. Macek, Comparison of different one-parameter damage laws and local stress-strain approaches in multiaxial fatigue life assessment of notched components, *International Journal of Fatigue* 151 (2021) 106405. doi:10.1016/j.ijfatigue.2021.106405.
- [21] Q.-Y. Deng, S.-P. Zhu, X. Niu, G. Lesiuk, W. Macek, Q. Wang, Load path sensitivity and multiaxial fatigue life prediction of metals under non-proportional loadings, *International Journal of Fatigue* 166 (2023) 107281. doi:https://doi.org/10.1016/j.ijfatigue.2022.107281.
- [22] C. Santus, L. Romanelli, T. Grossi, P. Neri, L. Romoli, A. Lutey, M. Pedranz, M. Benedetti, Torsional-loaded notched specimen fatigue strength prediction based on mode I and mode III critical distances and fracture surface investigations with a 3d optical profilometer, *International Journal of Fatigue* 161 (2022) 106913. doi:10.1016/j.ijfatigue.2022.106913.
- [23] D. Liao, S.-P. Zhu, G. Qian, Multiaxial fatigue analysis of notched components using combined critical plane and critical distance approach, *International Journal of Mechanical Sciences* 160 (2019) 38–50. doi:10.1016/j.ijmecsci.2019.06.027.
- [24] L. Susmel, D. Taylor, A critical distance/plane method to estimate finite life of notched components under variable amplitude uniaxial/multiaxial fatigue loading, *International Journal of Fatigue* 38 (2012) 7–24. doi:10.1016/j.ijfatigue.2011.11.015.
- [25] B. Gillham, A. Yankin, F. McNamara, C. Tomonto, D. Taylor, R. Lupoi, Application of the Theory of Critical Distances to predict the effect of induced and process inherent defects for SLM Ti-6Al-4V in high cycle fatigue, *CIRP Annals* 70 (1) (2021) 171–174. doi:10.1016/j.cirp.2021.03.004.
- [26] M. Benedetti, C. Santus, S. Raghavendra, D. Lusuadi, F. Zanini, S. Carmignato, Multiaxial plain and notch fatigue strength of thick-walled ductile cast iron EN-GJS-600-3: Combining multiaxial fatigue criteria, theory of critical distances, and defect sensitivity, *International Journal of Fatigue* 156 (2022) 106703. doi:10.1016/j.ijfatigue.2021.106703.
- [27] A. T. Tadesse, S.-P. Zhu, D. Liao, B. Keshtegar, Cyclic plastic zone-based notch analysis and damage evolution model for fatigue life prediction of metals, *Materials & Design* 191 (2020) 108639. doi:10.1016/j.matdes.2020.108639.
- [28] J.-L. Chaboche, Continuum damage mechanics: Part I—General concepts, *Journal of Applied Mechanics*.
- [29] A. T. Tadesse, S.-P. Zhu, D. Liao, H.-Z. Huang, Cyclic plastic zone modified critical distance theory for notch fatigue analysis of metals, *Engineering Failure Analysis* 121 (2021) 105163. doi:10.1016/j.engfailanal.2020.105163.
- [30] J. Chaboche, Time-independent constitutive theories for cyclic plasticity, *International Journal of Plasticity* 2 (2) (1986) 149–188. doi:10.1016/0749-6419(86)90010-0.
- [31] E. Voce, The relationship between stress and strain for homogeneous deformations, 1948.
- [32] C. O. Frederick, P. J. Armstrong, A mathematical representation of the multiaxial Bauschinger effect, *Materials at High Temperatures* 24 (1) (2007) 1–26. doi:10.3184/096034007x207589.
- [33] M. Benedetti, C. Santus, Mean stress and plasticity effect prediction on notch fatigue and crack growth threshold, combining the theory of critical distances and multiaxial fatigue criteria, *Fatigue & Fracture of Engineering Materials & Structures* 42 (6) (2018) 1228–1246. doi:10.1111/ffe.12910.
- [34] R. Branco, P. A. Prates, J. D. Costa, F. Berto, A. Kotousov, New methodology of fatigue life evaluation for multiaxially loaded notched components based on two uniaxial strain-controlled tests, *International Journal of Fatigue* 111 (2018) 308–320. doi:10.1016/j.ijfatigue.2018.02.027.
- [35] S. K. Paul, S. Tarafder, Cyclic plastic deformation response at fatigue crack tips, *International Journal of Pressure Vessels and Piping* 101 (2013) 81–90. doi:https://doi.org/10.1016/j.ijpvp.2012.10.007.
URL https://www.sciencedirect.com/science/article/pii/S0308016112001457
- [36] S. K. Paul, Numerical models to determine the effect of soft and hard inclusions on different plastic zones of a fatigue crack in a C(T) specimen, *Engineering Fracture Mechanics* 159 (2016) 90–97. doi:https://doi.org/10.1016/j.engfracmech.2016.03.028.
URL https://www.sciencedirect.com/science/article/pii/S0013794416301345
- [37] J. Chaboche, On some modifications of kinematic hardening to improve the description of ratchetting effects, *International Journal of Plasticity* 7 (7) (1991) 661–678. doi:10.1016/0749-6419(91)90050-9.
- [38] J.-L. Chaboche, P. Kanouté, F. Azzouz, Cyclic inelastic constitutive equations and their impact on the fatigue life predictions, *International Journal of Plasticity* 35 (2012) 44–66. doi:10.1016/j.ijplas.2012.01.010.
- [39] S. Koo, J. Han, K. P. Marimuthu, H. Lee, Determination of Chaboche combined hardening parameters with dual backstress for ratcheting evaluation of AISI 52100 bearing steel, *International Journal of Fatigue* 122 (2019) 152–163. doi:10.1016/j.ijfatigue.2019.01.009.
- [40] M. Rezaiee-Pajand, S. Sinaie, On the calibration of the Chaboche hardening model and a modified hardening rule for uniaxial ratcheting prediction, *International Journal of Solids and Structures* 46 (16) (2009) 3009–3017. doi:10.1016/j.ijsolstr.2009.04.002.

- [41] C.-H. Lee, V. N. V. Do, K.-H. Chang, Analysis of uniaxial ratcheting behavior and cyclic mean stress relaxation of a duplex stainless steel, *International Journal of Plasticity* 62 (2014) 17–33. doi:10.1016/j.ijplas.2014.06.008.
- [42] S. Liu, G. Liang, Y. Yang, A strategy to fast determine Chaboche elasto-plastic model parameters by considering ratcheting, *International Journal of Pressure Vessels and Piping* 172 (2019) 251–260. doi:10.1016/j.ijpvp.2019.01.017.
- [43] A. H. Mahmoudi, S. M. Pezeshki-Najafabadi, H. Badnava, Parameter determination of Chaboche kinematic hardening model using a multi objective Genetic Algorithm, *Computational Materials Science* 50 (3) (2011) 1114–1122. doi:10.1016/j.commatsci.2010.11.010.
- [44] D. Agius, M. Kajtar, K. I. Kourousis, C. Wallbrink, C. H. Wang, W. Hu, J. Silva, Sensitivity and optimisation of the Chaboche plasticity model parameters in strain-life fatigue predictions, *Materials & Design* 118 (2017) 107–121. doi:10.1016/j.matdes.2017.01.027.
- [45] N. Moslemi, M. G. Zardian, A. Ayob, N. Redzuan, S. Rhee, Evaluation of Sensitivity and Calibration of the Chaboche Kinematic Hardening Model Parameters for Numerical Ratcheting Simulation, *Applied Sciences* 9 (12) (2019) 2578. doi:10.3390/app9122578.
- [46] Q. T. Pham, D.-T. Nguyen, Parameter Identification of Chaboche Model for Aluminum Alloy Sheets Based on Differential Evolution Algorithm, *Journal of Advanced Engineering and Computation* 6 (3) (2022) 224. doi:10.55579/jaee.202263.375.
- [47] C. Santus, T. Grossi, L. Romanelli, M. Pedranz, M. Benedetti, A computationally fast and accurate procedure for the identification of the Chaboche isotropic-kinematic hardening model parameters based on strain-controlled cycles and asymptotic ratcheting rate, *International Journal of Plasticity* 160 (2023) 103503. doi:10.1016/j.ijplas.2022.103503.
- [48] C. Santus, L. Romanelli, T. Grossi, L. Bertini, P. Neri, L. L. Bone, F. Chiesi, L. Tognarelli, Investigation of Chaboche and Bouc–Wen Parameters of Quenched and Tempered Steel and Comparison of Model Predictive Capabilities, *Applied Sciences* 13 (5) (2023) 2961. doi:10.3390/app13052961.
- [49] Y. Lv, L. Lei, L. Sun, Effect of shot peening on the fatigue resistance of laser surface melted 20CrMnTi steel gear, *Materials Science and Engineering: A* 629 (2015) 8–15. doi:10.1016/j.msea.2015.01.074.
- [50] S. Héctor E Jaramillo, N. A. de Sánchez, D. Julian A Avila, Effect of the shot peening process on the fatigue strength of SAE 5160 steel, *Proceedings of the Institution of Mechanical Engineers, Part C: Journal of Mechanical Engineering Science* 233 (12) (2018) 4328–4335. doi:10.1177/0954406218816349.
- [51] S. Žagar, B. Markoli, I. Naglič, R. Šturm, The Influence of Age Hardening and Shot Peening on the Surface Properties of 7075 Aluminium Alloy, *Materials* 14 (9) (2021) 2220. doi:10.3390/ma14092220.
- [52] H.-z. Zheng, S.-h. Guo, Q.-h. Luo, X.-y. Shu, G.-f. Li, Effect of shot peening on microstructure, nanocrystallization and microhardness of Ti–10V–2Fe–3Al alloy surface, *Journal of Iron and Steel Research International* 26 (1) (2019) 52–58. doi:10.1007/s42243-018-0206-0.
- [53] S. Bagherifard, I. Fernandez-Pariente, R. Ghelichi, M. Guagliano, Effect of severe shot peening on microstructure and fatigue strength of cast iron, *International Journal of Fatigue* 65 (2014) 64–70. doi:10.1016/j.ijfatigue.2013.08.022.
- [54] E. Maleki, G. H. Farrahi, K. R. Kashyzadeh, O. Unal, M. Gugliano, S. Bagherifard, Effects of Conventional and Severe Shot Peening on Residual Stress and Fatigue Strength of Steel AISI 1060 and Residual Stress Relaxation Due to Fatigue Loading: Experimental and Numerical Simulation, *Metals and Materials International* 27 (8) (2020) 2575–2591. doi:10.1007/s12540-020-00890-8.
- [55] T. Mura, *Micromechanics of defects in solids*, Springer Netherlands, 1987. doi:10.1007/978-94-009-3489-4.
- [56] A. M. Korsunsky, The modelling of residual stresses due to surface peening using eigenstrain distributions, *The Journal of Strain Analysis for Engineering Design* 40 (8) (2005) 817–824. doi:10.1243/030932405x30984.
- [57] A. M. Korsunsky, K. M. Kim, G. M. Regino, Residual Stress Analysis in Shot Peened and Fretting Fatigued Samples by the Eigenstrain Method, *Materials Science Forum* 524-525 (2006) 343–348. doi:10.4028/www.scientific.net/msf.524-525.343.
- [58] A. M. Korsunsky, Residual elastic strain due to laser shock peening: Modelling by eigenstrain distribution, *The Journal of Strain Analysis for Engineering Design* 41 (3) (2006) 195–204. doi:10.1243/03093247jsa141.
- [59] A. M. Korsunsky, Residual Elastic Strains in Autofretted Tubes: Elastic–Ideally Plastic Model Analysis, *Journal of Engineering Materials and Technology* 129 (1) (2006) 77–81. doi:10.1115/1.2400267.
- [60] A. M. Korsunsky, W. J. J. Vorster, S. Y. Zhang, M. Topić, A. M. Venter, A beam-bending eigenstrain analysis of residual elastic strains in multi-scan laser-formed steel samples, *Proceedings of the Institution of Mechanical Engineers, Part C: Journal of Mechanical Engineering Science* 222 (9) (2008) 1635–1645. doi:10.1243/09544062jmes750.
- [61] A. M. Korsunsky, G. M. Regino, D. Nowell, Variational eigenstrain analysis of residual stresses in a welded plate, *International Journal of Solids and Structures* 44 (13) (2007) 4574–4591. doi:10.1016/j.ijsolstr.2006.11.037.
- [62] T.-S. Jun, A. M. Korsunsky, Evaluation of residual stresses and strains using the Eigenstrain Reconstruction Method, *International Journal of Solids and Structures* 47 (13) (2010) 1678–1686. doi:10.1016/j.ijsolstr.2010.03.002.
- [63] E. Salvati, A. J. G. Lunt, S. Ying, T. Sui, H. J. Zhang, C. Heason, G. Baxter, A. M. Korsunsky, Eigenstrain reconstruction of residual strains in an additively manufactured and shot peened nickel superalloy compressor blade, *Computer Methods in Applied Mechanics and Engineering* 320 (2017) 335–351. doi:10.1016/j.cma.2017.03.005.
- [64] M. Achintha, D. Nowell, Eigenstrain modelling of residual stresses generated by laser shock peening, *Journal of Materials Processing Technology* 211 (6) (2011) 1091–1101. doi:10.1016/j.jmatprotec.2011.01.011.
- [65] A. M. Korsunsky, J. Guénolé, E. Salvati, T. Sui, M. Mousavi, A. Prakash, E. Bitzek, Quantifying eigenstrain distributions induced by focused ion beam damage in silicon, *Materials Letters* 185 (2016) 47–49. doi:10.1016/j.matlet.2016.08.111.
- [66] A. M. Korsunsky, E. Salvati, A. G. J. Lunt, T. Sui, M. Z. Mughal, R. Daniel, J. Keckes, E. Bemporad, M. Sebastiani, Nanoscale residual stress depth profiling by Focused Ion Beam milling and eigenstrain analysis, *Materials & Design* 145 (2018) 55–64. doi:10.1016/j.matdes.2018.02.044.
- [67] M. Benedetti, V. Fontanari, B. D. Monelli, Numerical Simulation of Residual Stress Relaxation in Shot Peened High-Strength Aluminum Alloys Under Reverse Bending Fatigue, *Journal of Engineering Materials and Technology* 132 (1). doi:10.1115/1.3184083.
- [68] M. Marini, V. Fontanari, M. Benedetti, DEM/FEM simulation of the shot peening process on sharp notches, *International Journal of Mechanical Sciences* 204 (2021) 106547. doi:10.1016/j.ijmecsci.2021.106547.

- [69] S. Bagherifard, M. Guagliano, Application of different fatigue strength criteria on shot peened notched parts. part 2: nominal and local stress approaches, *Applied Surface Science* 289 (2014) 173–179. doi:10.1016/j.apsusc.2013.10.130.
- [70] M. Benedetti, V. Fontanari, M. Bandini, D. Taylor, Multiaxial fatigue resistance of shot peened high-strength aluminum alloys, *International Journal of Fatigue* 61 (2014) 271–282. doi:10.1016/j.ijfatigue.2013.10.020.
- [71] M. Benkhettab, H. Guechichi, S.-E. Benkabouche, Fatigue strength prediction methodology of shot-peened materials, *The International Journal of Advanced Manufacturing Technology* 104 (9-12) (2019) 4277–4287. doi:10.1007/s00170-019-04089-z.
- [72] M. Benedetti, V. Fontanari, C. Santus, M. Bandini, Notch fatigue behaviour of shot peened high-strength aluminium alloys: Experiments and predictions using a critical distance method, *International Journal of Fatigue* 32 (10) (2010) 1600–1611. doi:10.1016/j.ijfatigue.2010.02.012.
- [73] M. Benedetti, V. Fontanari, M. Allahkarami, J. C. Hanan, M. Bandini, On the combination of the critical distance theory with a multiaxial fatigue criterion for predicting the fatigue strength of notched and plain shot-peened parts, *International Journal of Fatigue* 93 (2016) 133–147. doi:10.1016/j.ijfatigue.2016.08.015.
- [74] S. Bagherifard, C. Colombo, M. Guagliano, Application of different fatigue strength criteria to shot peened notched components. Part 1: Fracture Mechanics based approaches, *Applied Surface Science* 289 (2014) 180–187. doi:10.1016/j.apsusc.2013.10.131.
- [75] B. Atzori, P. Lazzarin, G. Meneghetti, A unified treatment of the mode I fatigue limit of components containing notches or defects, *International Journal of Fracture* 133 (1) (2005) 61–87. doi:10.1007/s10704-005-2183-0.
- [76] UNI. (2008). UNI EN 15305: Non-destructive testing. Test method for residual stress analysis by X-ray diffraction.
- [77] S. K. Paul, Correlation between endurance limit and cyclic yield stress determined from low cycle fatigue test, *Materialia* 11 (2020) 100695. doi:https://doi.org/10.1016/j.mtla.2020.100695.